A. ALABISH

ATILIM UNIVERSITY 2019

MODELING AND CHARACTERIZATION OF HUMAN BODY SHADOWING AT MILLIMETER WAVES

THE GRADUATE SCHOOL OF NATURAL AND APPLIED SCIENCES
OF
ATILIM UNIVERSITY

AHMED ALABISH

DOCTOR OF PHILOSOPHY THESIS
IN
MODELING AND DESIGN OF ENGINEERING SYSTEMS (MAIN FIELD OF STUDY: ELECTRICAL AND ELECTRONICS ENGINEERING)

DECEMBER 2019

MODELING AND CHARACTERIZATION OF HUMAN BODY SHADOWING AT MILLIMETER WAVES

A THESIS SUBMITTED TO
THE GRADUATE SCHOOL OF NATURAL AND APPLIED SCIENCES
OF
ATILIM UNIVERSITY

BY

AHMED ALABISH

IN PARTIAL FULFILLMENT OF THE REQUIREMENTS
FOR
THE DEGREE OF DOCTOR OF PHILOSOPHY
IN
THE DEPARTMENT OF MODELING AND DESIGN OF ENGINEERING SYSTEMS (MAIN FIELD OF STUDY: ELECTRICAL AND ELECTRONICS ENGINEERING)

DECEMBER 2019

Approval of the Graduate School of Natural and Applied Sciences, Atilim University.

Prof. Dr. Ali Kara
Director

I certify that this thesis satisfies all the requirements as a thesis for the degree of **Doctor of Philosophy in Modeling and Design of Engineering Systems, Atilim University**.

Prof. Dr. Ender Keskinkılıç
Head of Department

This is to certify that we have read the thesis MODELING AND CHARACTERIZATION OF HUMAN BODY SHADOWING AT MILLIMETER WAVES submitted by AHMED ALABISH and that in our opinion it is fully adequate, in scope and quality, as a thesis for the degree of Doctor of Philosophy.

Asst. Prof. Dr. Yaser Dalveren
Co-supervisor

Prof. Dr. Ali Kara
Supervisor

Examining Committee Members:

Prof. Dr. Bülent Tavlı
Electrical and Electronics Eng. Dept., TOBB ETÜ

Prof. Dr. Ali Kara
Electrical and Electronics Eng. Dept., Atilim University

Prof. Dr. Elif Aydın
Electrical and Electronics Eng. Dept., Atilim University

Prof.Dr. Kemal Bıçakçı
Computer Engineering Department, TOBB ETÜ

Assoc. Prof. Dr. Murat Hüsnü Sazlı
Electrical and Electronics Eng. Dept., Ankara University

Date: 27/12/2019

I hereby declare that all information in this document has been obtained and presented in accordance with academic rules and ethical conduct. I also declare that, as required by these rules and conduct, I have fully cited and referenced all material and results that are not original to this work.

Name, Last Name: Ahmed, ALABISH

Signature :

ABSTRACT

MODELING AND CHARACTERIZATION OF HUMAN BODY SHADOWING AT MILLIMETER WAVES

Ahmed, Alabish

Phd, Department of Modeling and Design of Engineering Systems

Supervisor: Prof. Dr. Ali Kara

Co-supervisor: Asst. Prof. Dr. Yaser Dalveren

December 2019, 56 pages

As 5G communication may use Millimetre waves (mmWave) bands, it is essential to estimate short range indoor links from blockage point of view. This study presents some initial studies for characterizing effects of human body movement on short range link. To the best of our knowledge, this study is the first to experimentally examine the effects of human body movement at this band. This study also presents a simple approach to characterize the effects of scattering objects around indoor links at 28 GHz while the link is fully blocked by human body. The effects of scattering objects close to the link were carried out by performing measurements with a metallic reflector and human body. Here, fundamental mechanisms of wave propagation such as reflection and diffraction were accounted for each scattering object. To predict the attenuation produced by metallic reflector, specular reflection model was used in reflection modelling. In diffraction modelling, on the other hand, the double knife-edge diffraction (DKED) model was exploited to predict the attenuation by human body. Simulations were then compared with measurements to estimate the prediction accuracy of the models. Results indicate that presented simple models work well for indoor links. Therefore, the results of this study could be extended to model multiple human body near the indoor links of fifth generation (5G) systems.

Keywords: 5G, millimetre wave, human blockage, environmental blockage, double knife-edge diffraction.

ÖZ

MILIMETRE DALGALARINDA İNSAN VÜCUDU GÖLGELEMESİNİN MODELLENMESİ VE KARAKTERİZE EDİLMESİ

Alabish, Ahmed
Doktora, Mühendislik Sistemlerinin Modellenmesi ve Tasarımı Bölümü
Tez Yöneticisi: Prof. Dr. Ali Kara
Ortak Tez Yöneticisi: Asst. Prof. Dr. Yaser Dalveren

Aralık 2019, 56 sayfa

5G haberleşmesi Milimetre dalga (mmDalga) bantlarını kullanabileceği için kısa mesafe iç mekân haberleşme linklerinin blokaj açısından kestirimi önemli bir yer tutmaktadır. Bu çalışma kısa mesafe iç mekân haberleşme linklerindeki insan vücudu hareketinin etkilerini karakterize etmek için yapılan bazı ön çalışmaları sunmaktadır. Bildiğimiz kadarıyla, bu çalışma insan vücudu hareketinin bu bant aralığında etkilerini deneysel olarak inceleyen ilk çalışmadır. Bu çalışma ayrıca 28 GHz'de bir insan vücudu tarafından bloklanan bir iç mekân haberleşme linkinin çevresindeki yansıtıcı nesnelerin etkisini karakterize etmek için basit bir yaklaşım sunmaktadır. Metal reflektör ve insan vücudu ile ölçümler yapılarak linke yakın yansıtıcı nesnelerin etkisi irdelenmiştir. Burada, yansıma ve kırınım gibi dalga yayılımının temel mekanizmaları her bir yansıtıcı nesne için hesaba katılmıştır. Metalik reflektör tarafından üretilen zayıflamayı tahmin etmek için yansıma modellemesinde düzgün yansıma modeli kullanılmıştır. Kırınım modellemesinde ise, öte yandan, insan vücudunun neden olduğu zayıylamayı tahmin etmek için Çift Bıçak Kenarlı Kırınım (ÇBKK) modelinden faydalanılmıştır. Sonrasında modellerin tahmin doğruluğunu kestirebilmek için benzetimler ile ölçümler karşılaştırılmıştır. Sonuçlar sunulan basit modellerin iç mekân haberleşme linkleri için düzgün çalıştığını göstermektedir.

Dolayısıyla, bu çalışma beşinci nesil (5G) sistemlerin iç mekân haberleşme linkleri yakınındaki çoklu insan vücudunu modellemek için genişletilebilir.

Anahtar Kelimeler: 5G, milimetre dalga, insan blokajı, çevresel blokaj, çift bıçak kenarlı kırınım.

I dedicate this thesis to my family

ACKNOWLEDGMENTS

I would like to express my appreciation and thanks to my supervisor Prof. Dr. Ali Kara for his guidance, advice and encouragement.

To my co-supervisor Asst. Prof. Dr. Yaser Dalveren, I would like to express my appreciation for his guidance and helping.

Furthermore, I would like to extend my deepest gratitude to my committee members, Prof.Dr. Kemal Bıçakçı and Assoc Prof. Dr. Murat Hüsnü Sazlı. My deep appreciation goes out to the members of my examination Prof. Dr. Bülent Tavlı and Prof. Dr. Elif Aydın.

To my wife, I offer sincere thanks for her support.

The financial support of The Ministry of Education Libya is also acknowledged.

TABLE OF CONTENTS

LIST OF TABLES

TABLES

LIST OF FIGURES

FIGURES

FIGURES

LIST OF SYMBOLS/ABBREVIATIONS

dB	decibel
DKED	Double Knife-Edge Diffraction model
G	Generation
GTD	Geometrical Theory of Diffraction
HBS	Human Body Shadowing
KED	Knife Edge Diffraction
LOS	Line of Sight
mm Wave	Millimeter waves
NLOS	Non-Line of Sight
VNA	Vector Network Analyzer
1G	First generation
2G	Second generation
3 G	Third generation
4G	Fourth generation
5G	Fifth generation

CHAPTER 1

INTRODUCTION

Nowadays with developing technology, the use of smart phones and tablets has become widespread among people. This allows them to get whatever they want from the internet easily. The availability of various social network websites, on the other hand, attracts people to exchange the data (sharing pictures, downloading videos, etc.), leads to an unprecedented increase in demand for high data rates. In this context, wireless communication has followed different evolutionary paths. These evolutionary paths aimed at unified target related to efficiency and performance in different environment.

Generation (G) generally denotes to a change in the essential nature of the service, and new frequency bands. It is widely known that (1G) the first generation of wireless system, was used for speech services. A few years later, the second generation (2G) appeared. The main feature of the 2G is digital broadcasting system instead of analog broadcasting. Then, Wide Band Wireless Network (WBWN) was used in the third generation (3G). It is better than the 1G and 2G when it is compared in terms of speed, capacity, efficiency and video calling capabilities. Finally, in 2005 a fourth generation (4G) appeared, which is still used so far. It is ten times faster than 3G, which provides high-resolution video transmission [1]. However, the user's daily service has been increased, and a lot of data has been transmitted between the devices. Some services need a high data rate to increase their efficiency and performance, which led us the need for a new technology.

Every day a huge amount of data is used (smartphones, smart TV, etc.) by users. Therefore, a large number of synchronized connections are connected (servers) to satisfy this demand for higher data rates. However, networks still have some data rate limitations for many service. More efficient and lower energy consumption is required. A fifth generation (5G) will fulfill the end-users demands, and will be able to connect a billions of devices efficiently. The frequency band will be millimeter-wave band, which is approximately between 30 GHz and 300 GHz. This band allows larger

bandwidth allocations. 5G does not only increase connection speed, but also cover the way for a smart connection. It allows devices to connect more efficiently between themselves. 5G includes all type of advanced features, which makes it powerful, to eliminate the data rate limitations of telecommunications services. This technology is still in development phase [2].

1.1. Research Background

Although millimeter wave systems offer efficient communication link to end-users, the efficiency is quite sensitive to blockage problem. This is because millimeter signals have quite short wavelengths, typically around 5 mm. In addition, the transmission loss in indoor environment is very high at millimeter wave frequencies due to obstacles (people, walls, furniture, etc.). Blockage problem almost occurs in indoor environment. Especially in crowded places, such as shopping malls, store fronts, and airports. For this reason, analyzing the conditions of the local environment for short indoor connections becomes significant to evaluate the performance of 5G systems. Particularly, the effects of human body shadowing, which is the shadow fading occurred when humans crossing the LOS path between the receiver and the transmitter, should be necessarily studied at millimeter. Path loss is a fundamental part in the investigation of the indoor environment propagation. It is the loss of power of a travelling signal through the space which is expressed in decibel (dB).

In [3], it is obvious that the path loss is increased when the radio frequency is increased. This phenomenon gives rise to slight coverage of millimeter communication. To overcome the increased path loss, directional antennas are used [4]. However, it is still the major component in the analysis of the channel propagation. The path loss depends on the distance among transmitting antenna and receiving antenna, clearance of Line of Sight (LOS) which is a direct path between the transmitter and the receiver, and antenna's height.

Evidently, the transmitted signal may have reached the receiver side either LOS or Non-Line of Sight (NLOS). The received signal of LOS propagation in indoor environment consists of LOS signal and multipath components. Furthermore, the transmitted signal arrives at the receiver, from various paths, each with different magnitude, and phase. Then, the result could be constructive interference or

destructive interference. When the signals are at same phase and direction, this is called as constructive interference, otherwise destructive interference [5]. In NLOS case, the transmission loss is very high. The received signal may be exposed to diffraction, reflection and scattering from objects nearby the transmission link [6].

Moreover, people are the most influential object on the communication channel in the indoor environment. Movement of people is unstable in one place, and the height of the antennas may not be so high. Thus the LOS may be blocked by people many times. The effects of human bodies at millimeter wave are investigated by several studies[7]. However, limited works have considered measurements to assess the effects of human blockage at 28 GHz. The following section provides a brief discussion on these studies.

1.2. Literature Review

In [8] the attenuations of human bodies had investigated at 26 and 39.5 GHz. The measurements was done by using a time-domain channel sounder with horn-to-horn antennas. In theory Meanwhile, Vogler's multiple knife-edge model was applied to predict the attenuations.

Likewise, human body shadowing measurements have conducted in [9]. Measurements were achieved by wideband channel sounder, a center frequency of 28 GHz with the bandwidth of 800 MHz. In the measurements, horn antennas with their 1.3 m heights were used. Human Body Shadowing (HBS) model depends on three parts: a) geometric model of human body, b) process of computing shadowing gain and c) the phase correction. The multiple-edge diffraction is used to calculate the total received power. The Fresnel diffraction method has been used to define the effect of diffraction. A least mean square error method was used for the phase correction. Finally, the measurement results of gain has been observed between 6.29 dB and 15.62 dB, and gain of HBS model in general is 10 dB or a little more.

Other study presents human blockage at millimeter wave by using a simple Double Knife-Edge Diffraction model (DKED) [10]. It presents a human blockage at centered 73 GHz with 1 GHz bandwidth, where the transmitted power was -5.8 dBm. The transmitter and receiver were directional antennas with 20 dBi gain and 1.4 m height. The receiver was located 5 m away from the transmitter. A person (the human blocker) walked from through the LOS link. A DKED simulates human blocker as a screen of

two sides. It considers only the side edges for diffraction. A numerical approximation of DKED was developed which is called as METIS human blockage model in order to evaluate the results. The result of the DKED model, METIS human blockage model and measurement power were compared. It was shown that 30 dB to 40 dB of attenuation for a single blocker could be obtained at this band.

In [11], the human body blockage measurements were carried out at 11, 16, 28, and 32 GHz. A Vector Network Analyzer (VNA) and two 20 dBi horn antennas were used in an indoor environment. Three scenarios were performed. In these scenarios, one person walks along the LOS, one person across the LOS, and two persons across the LOS. The METIS knife-edge diffraction (KED) model, Kirchhoff KED model, and geometrical theory of diffraction (GTD) model were used to calculate the human blockage effects. The Gaussian model was also performed to evaluate the measurement data. When the results are compared, 20 dB loss is caused by human blockage has been observed.

1.3. Aim and Objectives of the Study

As 5G communication may use millimeter wave bands, it is necessary to evaluate short-range indoor links from the link blockage point of view. On the other hand, only limited works have considered measurements to evaluate the effects of human blockage at 28 GHz. However, at this frequency band, no study has taken into account the effects of multiple blockages near the propagation link. In this context, to the best of our knowledge, the study presented in this thesis is the first report to provide a simple but accurate approach to characterize the effects of nearby objects around indoor links at 28 GHz while human body fully blocking the link. In the study, two scattering objects, a metallic reflector and human body, were considered. To do this, simple propagation models such as reflection and diffraction were incorporated. In diffraction modelling, DKED model was employed to predict the attenuation caused by human blockage(s) for the sake of simplicity. In reflection modelling, specular reflection model was used to predict the attenuation due to metallic reflector. The accuracy of the models were then evaluated by comparing the simulations with the measured received powers. The results show that even these simple models may work well for simplistic indoor links. Especially, the diffraction model of human body

scattering provides acceptable results. Thus, the results obtained in this study may encourage the researchers to study modelling of people blocking and moving nearby the links in future 5G wireless systems.

1.4. Thesis Structure

In chapter 2 some information about radio signal propagation are induced, also it includes commonly diffraction models of human body. Chapter 3 explains system measurement and environment, initial preparing measurement, initial measurements are discussed, and the accurate system measurement is chosen, a simple model is performed in chapter 4 includes the results and discussions. Finally, the conclusion is included in the chapter 5.

CHAPTER 2

SIGNAL PROPAGATION AND HUMAN BODY MODELS

With the increasing of mobile traffic demand the contradiction between capacity requirements and spectrum shortage becomes notable. The bottleneck of wireless bandwidth will be the main problem for the 5G wireless networks. Thus, with huge bandwidth in the millimeter wave band from 30 GHz to 300 GHz, as explained in Figure 2.1, millimeter wave communications are proposed to be an important part of the next generation [12]. However, the final success of these efforts is based on based on system designs that account for the basic variation among millimeter wave connection, and current wireless networks at lesser carrier frequencies [13].

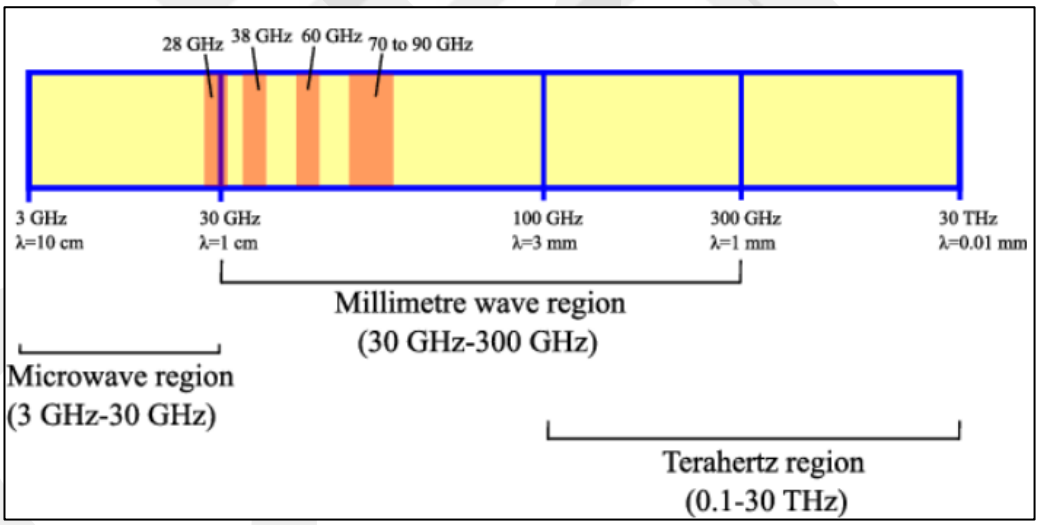

Figure 2.1. Millimeter wave region of the electromagnetic spectrum [14].

Although millimeter wave systems offer efficient communication link to end-users, their transmissions suffer from high path loss. In general, the overall loss of millimeter systems is large when compared with those of microwave systems for a point-to-point link. Therefore, there are many challenges for millimeter communications to make a significant impact on 5G. Directivity and sensitivity to blockage of millimeter communications need new thoughts, to handle these challenges. Millimeter wave links

are inherently directional, because it's a small wavelength, as shown in figure 2.2. Directional antennas are used to reduce the high path loss [15, 16].

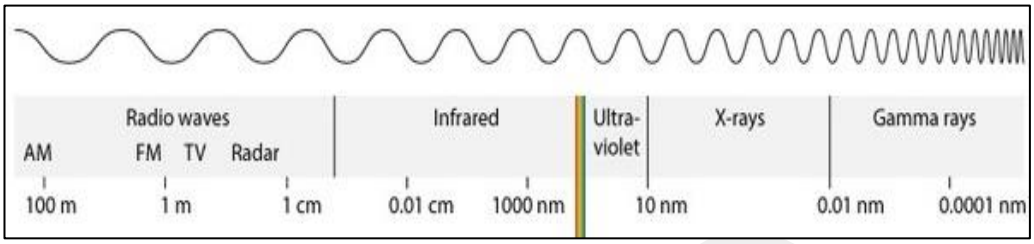

Figure 2.2. Wavelengths of different types of radiation [17].

Sensitivity to blockage is the most important challenge of millimetre communications. The potential of electromagnetic waves to diffract around objects whose diameter is significantly greater than the wavelength is very small. Therefore, since the wavelength of millimetre waves in average is 5 mm, links are effectively blocked by objects, especially in indoor environments. For example, human activity in a room can cause intermittent blockages of millimetre communication links. Thus, evaluating environmental conditions becomes important to assess the performance of 5G communication systems, especially in indoor environments. Facing such a challenge needs models that take diffraction into account in order to gain insight into the design and evaluate the performance.

2.1. Signal Propagation

Propagation models in indoor environments commonly focus on estimating the average received signal strength at a given distance, from a transmitter in addition to the fluctuation of the signal strength. The free space propagation model is applied to estimate received signal strength when the transmitter has a clear LOS with the receiver. Multipath propagation models describe the varying mechanisms behind electromagnetic wave propagation. however, they mostly refer to reflection, diffraction and scattering [5].

2.1.1. Free Space Propagation

It is a propagation of a transmitted signal through free space to the receiver which is located at distance d away from the transmitter, as shown in the figure 2.3. Where

there are no obstructions between the transmitter and receiver, and the signal propagates along a LOS between the Rx and Tx. The path loss of the signal is defined as a dB value of the linear path loss, or equivalently the power variance between the signal transmitted and the signal received.

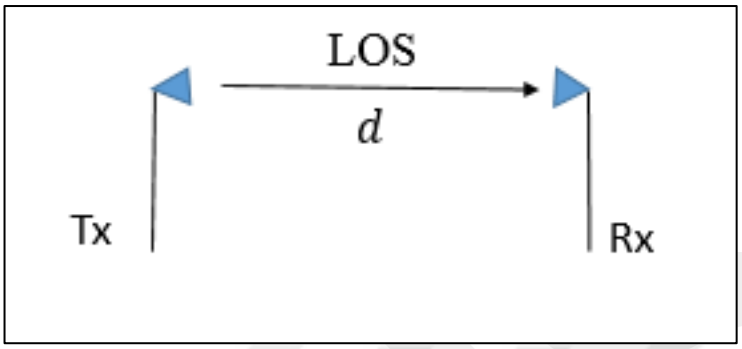

Figure 2.3. Free space propagation.

The received power of free space being received by a receiver antenna, which is located at distance d from radiating transmitter antenna, is given by the Friis space equation.

$$P_r(d) = \frac{P_t G_t G_r \lambda^2}{(4\pi)^2 d^2 L} \tag{2.1}$$

Furthermore, the loss of free space path can be expressed by the ratio of the transmitted power and the received signal power, or by the log of the ratio. [18].

$$FSPL = \frac{P_t}{P_r} = \frac{(4\pi d)^2}{\lambda^2} = \frac{(4\pi f d)^2}{c^2} \tag{2.2}$$

$$FSPL(dB) = 20\log(\frac{4\pi d}{\lambda}) \tag{2.3}$$

Where P_t is the transmitted power of the signal in watt, P_r is the received power of the signal in watt, G is the gain of the antennas, d is the distance in meter, λ is the wavelength of signal in meter, f is the frequency in hertz and c is the speed of light in space in meter per second. The received power can be calculated as:

$$P_r(dB) = P_t(dB) + Gt(dBi) + Gr(dBi) - FSPL(dB) \tag{2.4}$$

Where P_t is the transmitted power in dB, P_r is the received power in dB, Gt is the gain of the transmitted antenna in dBi, Gr is the gain of the received antenna in dBi, and $FSPL$ is the free space path loss in dB.

2.1.2. Multipath Propagation

Multipath propagation is a propagation phenomenon in which radio signals reach receiving antennas via more than one path, each path having a different attenuation, as shown in figure 2.4. However, the signal hits objects (human bodies, furniture, walls, etc.) nearby the LOS, resulting in physical phenomena such as reflection, diffraction and scattering being responsible for the production of different paths leading to the receiver antenna.

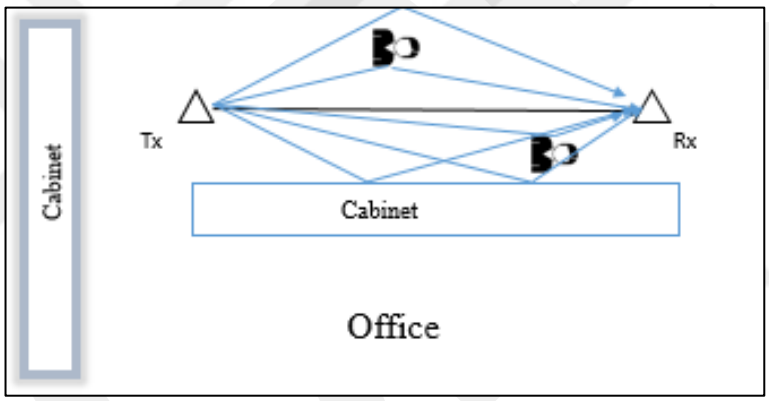

Figure 2.4. Multipath propagation in an indoor environment with a clear LOS.

Since the path that is the strongest in such a case is the LOS, it encourages restriction of LOS so as to maximize power efficiency [19]. However, it is not always possible to provide a clear LOS transmission. Furthermore, the multi-path can impact both LOS and NLOS. Non-line of sight is a phrase mostly used when the radio transmitter and receiver are not in direct visual line of sight, as shown in figure 2.5. Different paths are produced by the physical phenomena of reflection, diffraction and scattering, which are responsible for the propagation of the signal behind obstacle [20].

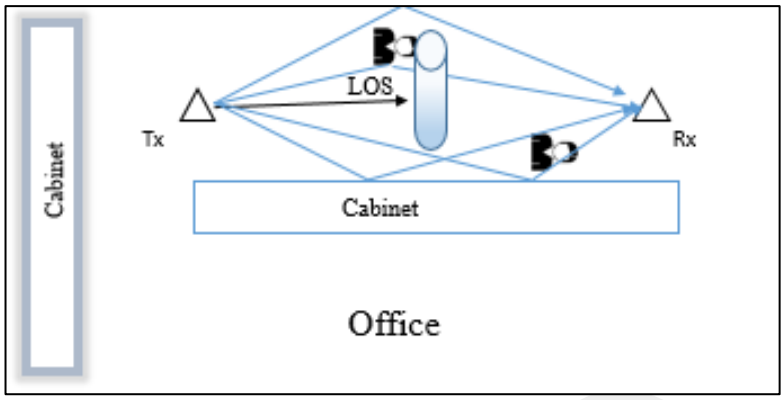

Figure 2.5. Multipath propagation with NLOS in indoor environment.

Reflection takes place when a propagating electromagnetic wave hits objects with has very large dimensions compared its wavelength. Scattering occurs when the medium through which the wave travels is made up of small objects, but it is large relative to the wavelength. Diffraction happens when an object with edges blocks the radio path between the transmitter and the receiver, and the secondary surface waves are present throughout the space behind the obstacle [21]. Reflection, scattering and diffraction are briefly described in the following section.

2.1.2.1. Reflection

When a radio wave propagates in one medium and then impinges upon another medium, with unlike properties, the wave will be partially reflected back and partially transmitted through the second medium. As shown in the figure 2.6, some of the power of the wave is reflected back to the first medium and some is transmitted to the other medium.

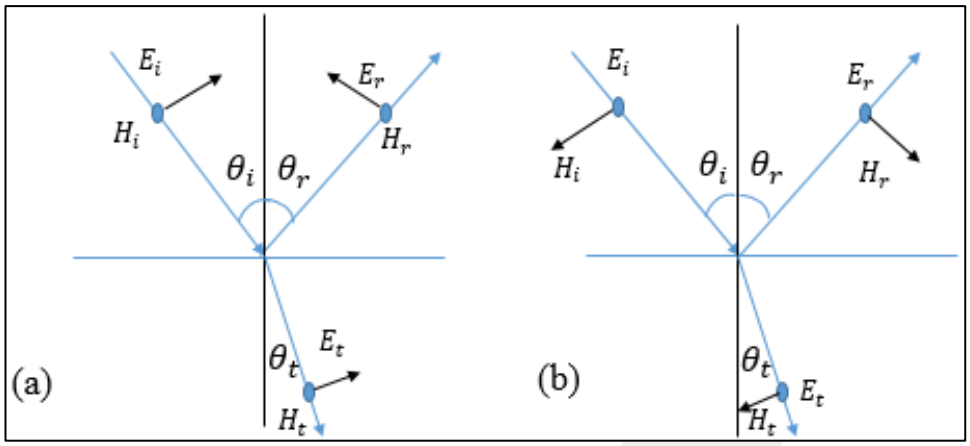

Figure 2.6. (a) Parallel polarizations. (b) Perpendicular polarizations.

The nature of the wave reflection depends on the electrical properties of the second medium, and if the propagating wave is incident on a perfect dielectric, most of the energy is transmitted to the second medium. If the propagating wave is incident on a perfect conductor, most of the energy is reflected back to the first medium. The reflection coefficient $r_{\perp\parallel}$ for two different media is given as [5].

$$\Gamma_{\parallel} = \frac{E_r}{E_i} = \frac{\eta_2 \sin\theta_t - \eta_1 \sin\theta_i}{\eta_2 \sin\theta_t + \eta_1 \sin\theta_i} \tag{2.5}$$

$$\Gamma_{\perp} = \frac{E_r}{E_i} = \frac{\eta_2 \sin\theta_t - \eta_1 \sin\theta_i}{\eta_2 \sin\theta_t + \eta_1 \sin\theta_i} \tag{2.6}$$

Where η_i is the impedance of i^{th} medium $(i = 1, 2)$, and is given by $\sqrt{\mu_i + \varepsilon_i}$.

When the first medium is free space, and $\mu_1 = \mu_2$, the reflection coefficient $\Gamma_{\perp\parallel}$ is given as

$$\Gamma_{\perp} = \frac{E_r}{E_i} = \frac{\cos\theta_i - \sqrt{\varepsilon^{"} - sin^2\theta_i}}{\cos\theta_i + \sqrt{\varepsilon^{"} - sin^2\theta_i}} \tag{2.7}$$

$$\Gamma_{\parallel} = \frac{E_r}{E_i} = \frac{-\varepsilon^{"} * \cos\theta_i - \sqrt{\varepsilon^{*} - sin^2\theta_i}}{\varepsilon^{"} * \cos\theta_i + \sqrt{\varepsilon^{*} - sin^2\theta_i}} \tag{2.8}$$

$$\varepsilon'' = \frac{\sigma}{2\pi f \varepsilon_0} \tag{2.9}$$

Where i, r, t indecate to the incident, reflected, and transmitted fields, respectively. $\varepsilon_i, \mu_i, \sigma_i$ are indicate to the permittivity, permeability, and conductivity of the two media. The boundary condition of Maxwell's equations are applied to derive (2.5) and (2.6) in addition to

$$\theta_i = \theta_r \tag{2.10}$$

$$E_r = \Gamma E_i \tag{2.11}$$

$$E_t = (1 + \Gamma) E_i \tag{2.12}$$

2.1.2.2. Scattering

The practical power level of the received signal in mobile environment is higher than what is foretell by only the reflection and diffraction models. The reason is that when a radio wave hits on a rough surface, its energy is mirrored and distributed by scattering in all directions. Surface roughness is mostly tested using the Rayleigh criterion, which determines a critical height h_c of surface protuberance for a given angle of incidence θ_i, given by

$$h_c = \frac{\lambda}{8 \sin \theta_i} \tag{2.13}$$

The surface is classified as a smooth surface if the height of its protuberance h is less than h_c [5]. Otherwise the smooth surface reflection coefficient has to be multiplied by a scattering loss factor ρ_S, to be considered for a reduced reflected field.

The height of its protuberance h on the surface is assumed to be Gaussian distributed random variable with a local mean [22], then ρ_S is given as

$$\rho_S = exp\left[-8\left(\frac{\pi \sigma_h \sin \theta_i}{\lambda}\right)^2\right] I_0\left[8\left(\frac{\pi \sigma_h \sin \theta_i}{\lambda}\right)^2\right] \tag{2.14}$$

Where σ_h is the standard deviation of the height protuberance h on the surface, and I_0 the Bessel function of the first kind and zero order. The rough surface can be solved as

$$\Gamma_{rough} = \rho_S \Gamma \tag{2.15}$$

2.1.2.3. Diffraction

A simple way to understand diffraction is through the Huygens-Fresnel principle, as shown in figure 2.4. A simple description of the Huygens-Fresnel principle is that every point on a propagating wavefront acts as the source of new spherical secondary wavelets (with the same frequency of the first wave) [23].

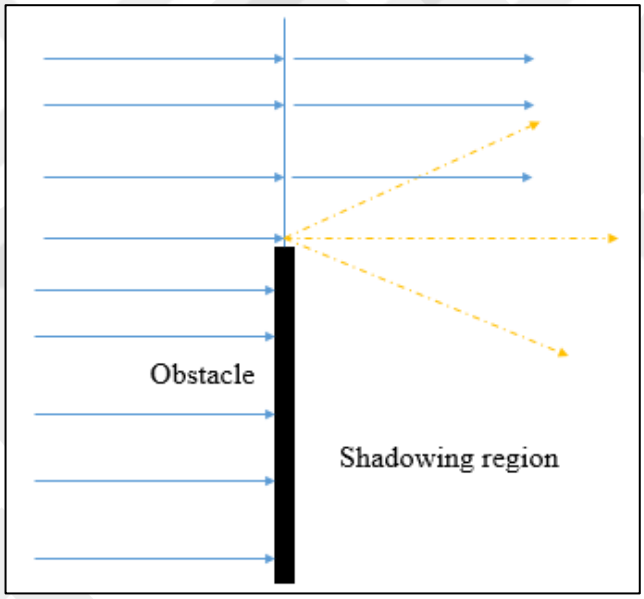

Figure 2.7. Plan wave encountering the edge of an obstacle.

Diffraction is produced with the propagation of secondary wavelets into a shadowed region. The strength of the field in the shadowed region is the total summation of the electric field component of the secondary wavelets in the space around the obstacle [5].

A knife edge geometry is a simple case of diffraction, where there as a transmitter and receiver in free space, and an obstruction screen of effective height with infinite width, being placed between them at distance d_1 from the transmitter, and at distance d_2 from the receiver as shown in figure 2.8.

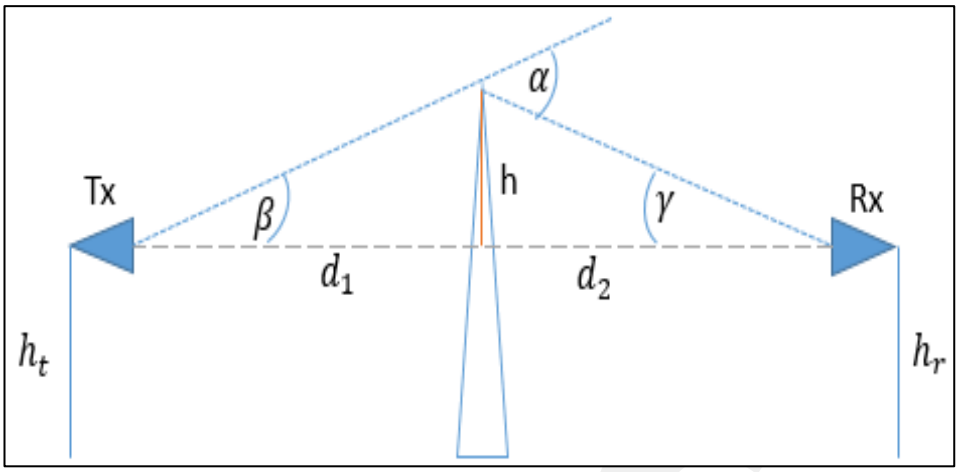

Figure 2.8. Knife edge geometry for single obstacle.

Based on the edge geometry diffraction in figure 2.4 the path difference Δ defined as

$$\Delta = \sqrt{d_1^2 + h^2} + \sqrt{d_2^2 + h^2} - (d_1 + d_2) \tag{2.16}$$

The approximate path length is,

$$\Delta \approx \frac{h^2(d_1+d_2)}{2d_1d_2} \tag{2.17}$$

since $h \ll d_1, d_2$. Hence the phase difference becomes,

$$\emptyset = \frac{2\pi}{\lambda}\Delta = \frac{\pi h^2(d_1+d_2)}{d_1d_2} \tag{2.18}$$

and

$$\alpha = \beta + \gamma \approx \tan\beta + \tan\gamma \tag{2.19}$$

Therefore, in radians,

$$\alpha \approx h\left(\frac{d_1+d_2}{d_1d_2}\right) \tag{2.20}$$

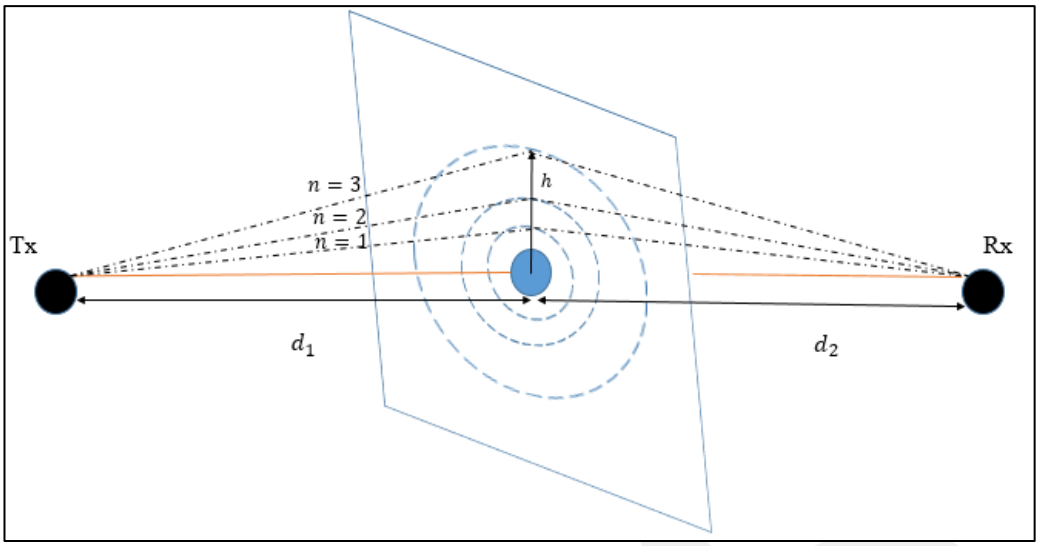

Figure 2.9. Fresnel zone.

It is significant to mention the Fresnel zone, since the obstacle that penetrate the first zone plays an important role in diffraction loss. A Fresnel ellipsoid is a surface where Δ is constant and has the value.

$$\Delta = n\frac{\lambda}{2} \tag{2.21}$$

Equation (2.18) is mostly normalized by using the Fresnel Kirchhoff diffraction parameter v which is given as

$$v = h\sqrt{\frac{2(d_1+d_2)}{\lambda d_1 d_2}} \tag{2.22}$$

Where n is integer as shown in figure 2.9, and is usually defined with its maximum radius r_n.

$$r_n = \sqrt{\frac{n\lambda d_1 d_2}{d_1+d_2}} \tag{2.23}$$

2.2. Human Body Models

Obstacles such as human bodies along with furniture cause blockage problem in the links. For this reason, the effects and characterization of human body blockage, on the

links at millimetre wave bands have been investigated, in several studies. most of which were on blockage problem, the knife edge diffraction (KED) model, geometrical theory for diffraction (GTD) and Gaussian model, are widely used to estimate attenuation due to human blockage. The theoretical value of the human body model and the path loss calculation are both used to predict the received power.

2.2.1. KED Model

The KED model adopts an absorbing rectangular screen to represent a human blocker. Three methods of the KED model are often used to estimate the losses caused by the human blockage effects. The first method is the METIS KED model [11], which is a numerical approximation developed by the METIS project. The second method is the Kirchhoff KED model [24, 25], which uses the Kirchhoff diffraction equation to calculate the losses. The third method is a simple DKED model [26, 27], a mathematical estimate for DKED established in the METIS human blockage model.

2.2.1.1. METIS KED Model

It is a mathematical estimate established by the METIS project. To simulate the human body a rectangular absorbing screen is used. It is vertical to the ground and its orientation is parallel to the Tx-Rx connecting line. The four edges of the screen are taken into account to calculate the loss as shown in Figure 2.10. The attenuation caused by the top edge (A_t) and the bottom edge (A_b) are calculated using the side projection view of the screen. The attenuation caused by the sides (the left edge (A_l) and the right edge (A_r)) are calculated using the top projection view of the screen.

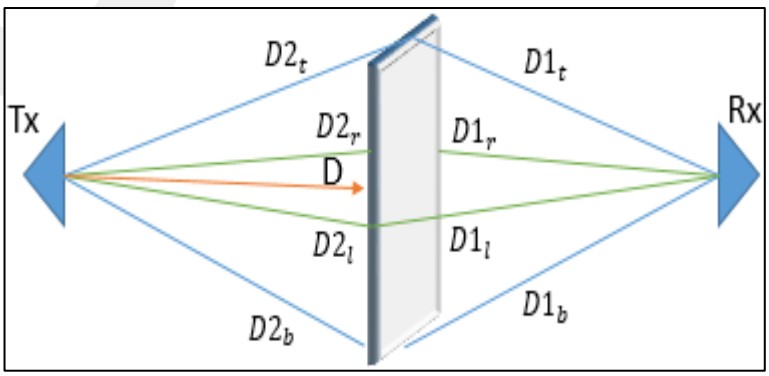

Figure 2.10. The METIS model.

The attenuation caused by each edge of the rectangular absorbing screen is calculated by using the following equation.

$$A = \frac{atan(\bar{+}\sqrt{\frac{\pi}{\lambda}((D_2+D_1)-D)})}{\pi} \quad (2.24)$$

Where A is E-field gain caused by diffraction, λ is the carrier wavelength, D_1 is the projection distances from the edge to the Rx antenna, D_2 the projection distance from the edge to the Tx and D the projection distance of LOS from the Tx to the Rx. the total loss is obtained by next equation.

$$L(dB) = -20\log_{10}(1-(A_l+A_r)(A_t+A_b)) \quad (2.25)$$

2.2.1.2. Kirchhoff KED Model

The Kirchhoff diffraction equation is used in the Kirchhoff KED model. It is used to simulate loss caused by human blockages. Figure 2.11 illustrates the aperture diffraction for the Kirchhoff KED model.

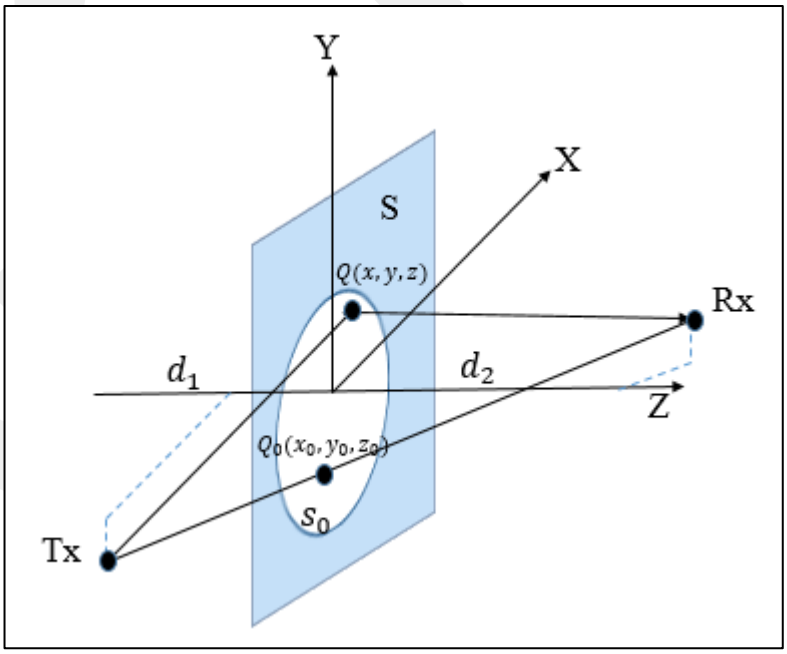

Figure 2.11. Aperture diffraction for the Kirchhoff KED model.

Where S is an infinity screen in the X-Y plane, S_0 denotes to the aperture on the screen, Q_0 is the joint point of the Tx and Rx connecting line with the aperture, d_1 and d_2 indicates the projection of Tx to Q_0 and Rx to Q_0 on Z axis, respectively. The first Fresnel zone radius can be calculated in a next equation.

$$R_1 = \sqrt{\lambda \frac{d_1 d_2}{d_1 + d_2}} \tag{2.26}$$

Using the Kirchhoff diffraction equation the attenuation caused by the aperture can be calculated as

$$A = F_d(u, v) = \frac{j}{2} \iint_{s_0} \exp\left[-j \frac{\pi}{2}(u^2 + v^2)\right] du dv \tag{2.27}$$

Where Fresnel number is found by a $F_d(u, v)$, the parameters u and v can be written as

$$u = \sqrt{2} \frac{x - x_0}{R_1}, \; v = \sqrt{2} \frac{y - y_0}{R_1} \tag{2.28}$$

Where $x - x_0$ is the distance from the Tx to the edge, and $y - y_0$ is the distance from the edge to the Rx as shown in Figure 2.11.

2.2.1.3. DKED Model

Although several accurate methods to estimate the attenuation due to human blockage have been proposed, among these models, namely the double knife-edge diffraction (DKED) model, is mathematically simple, accurately simulates the human blockage effects, and allows straightforward implementation.

In DKED modelling, human blockage is estimated by a square screen with infinite perpendicular height. Only the side edges of the screen are considered for diffraction. A typically the top-down projection of the blockage is shown in Figure 2.12.

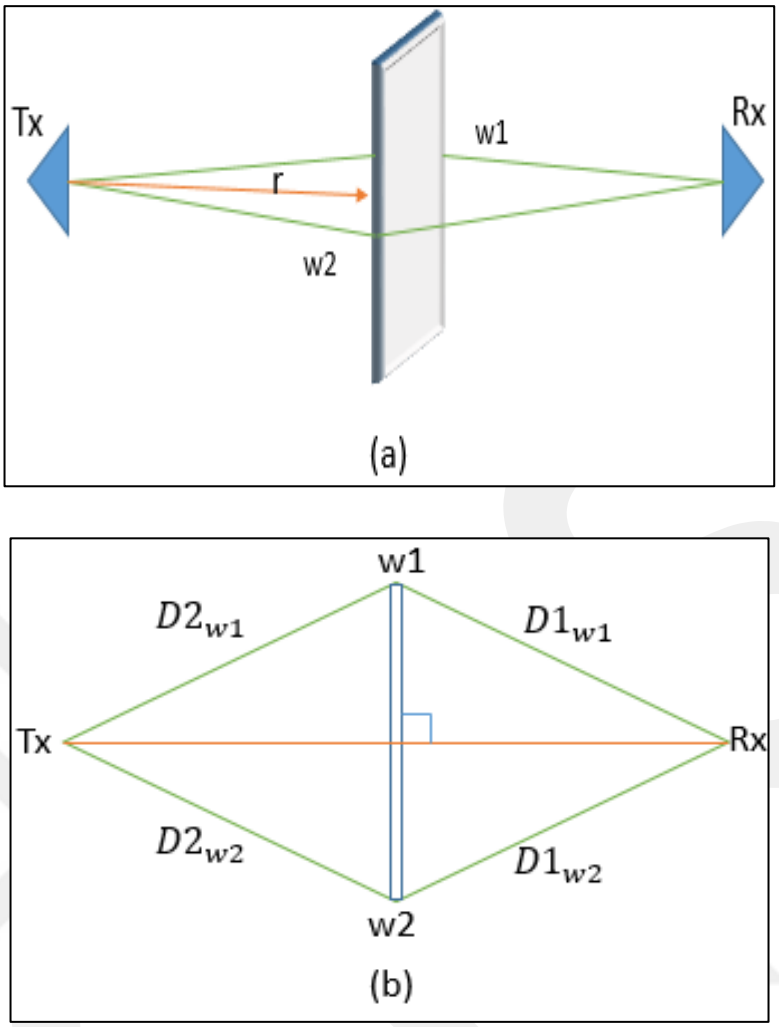

Figure 2.12. (a) 3D screen projection. (b)Top-down projection of the blockage.

Where w is the width of screen, r is the distance between the transmitter (Tx) and receiver (Rx), and $D_{1,2}$ are the dimensions. The corresponding shadowing incurred by each of the 2 edges (w1; w2) based on KED is determined as

$$\boldsymbol{F_{w1,w2}} = \frac{\tan^{-1}(\pm\sqrt{\frac{\pi}{\lambda}((D_{2w1,w2}+D_{1w1,w2})-r)}}{\pi} \tag{2.29}$$

Where F is E-field gain caused by diffraction, λ is the carrier wavelength, and D_W is the distances based on dimensions. The blockage loss by a blocker is modeled by screen with the two edges (w1, w2) as

$$SL = -20\log_{10}\left|\left(\frac{1}{2} - F_{w1}\right) \times \sqrt{G_{Txw1}(\theta)} \times \sqrt{G_{Txw2}(\theta)} + \left(\frac{1}{2} - F_{w2}\right) \times \sqrt{G_{Rxw1}(\theta)} \times \sqrt{G_{Rxw2}(\theta)}\right| \quad (2.30)$$

Here θ is the projected angle from the Tx to the edge ($w1$ or $w2$) as shown in figure 2.13. and from the edge ($w1$ or $w2$) to Rx, $G_{Txw1|Txw2|Rxw1|Rxw2}(\theta)$ (the subscript symbol "$*\,|\,\cdot$" denotes "$*$ or $\cdot$") are the normalized gains of the antennas based on θ relative to boresight gain.

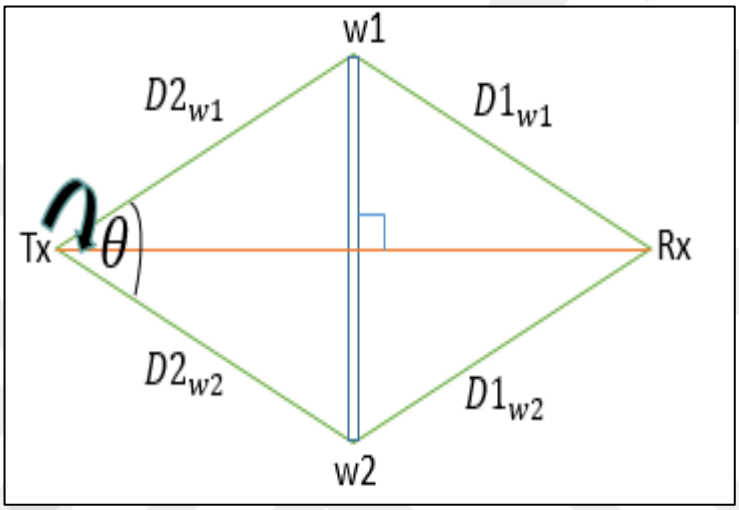

Figure 2.13.Top-view the projected angle from the Tx to the edge.

2.2.2. Geometrical Theory of Diffraction (GTD) Model

The GTD model is an expansion of geometrical optics considered for diffraction. It is used to simulate the human body as a perfectly conducting cylinder [28]. The plane wave at a circular cylinder is explained in Figure 2.14.

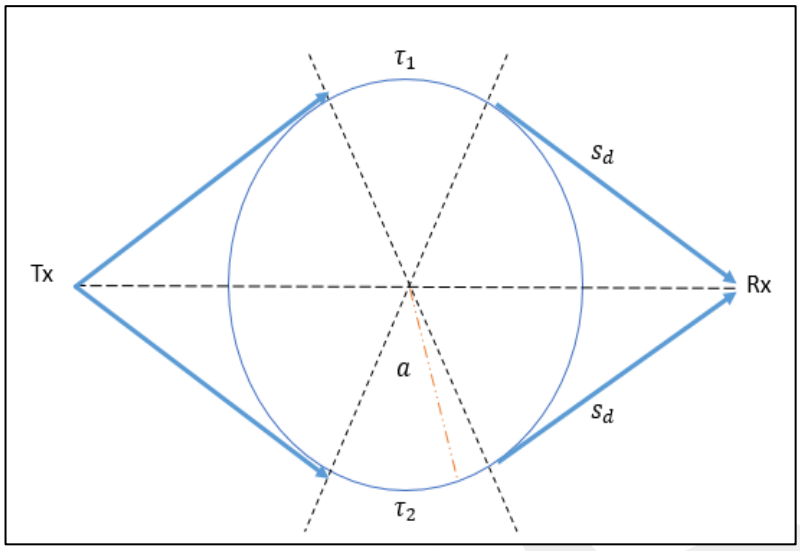

Figure 2.14. The GTD model.

The attenuation caused by the blockage effect can be written as

$$A = \sum_{n=1}^{N} D_n^e \frac{\exp(-jkS_d)}{\sqrt{8jkS_d}} \times \{\exp[-(jk + \Omega_n^e)\tau_1] + \exp[-(jk + \Omega_n^e)\tau_2]\} \quad (2.31)$$

Where N is the slected number of zeros of Airy function A, k is the wavenumber, S_d is the distance Rx antenna and the point tangency of the cylinder, Ω_n^e is the attenuation constant, τ_1 and τ_2 are the travel distances on the surface. D_n^e is the amplitude weighting factor, which can be calculated thus.

$$D_n^e = 2M\{A_{i'}(-\alpha_n)\}^2 e^{\frac{-\pi}{6}} \quad (2.32)$$

Where $A_{i'}$ is the derivative function of Airy function, $-\alpha_n$ is the zeros of Airy function and M parameter can be written as

$$M = (\frac{ka}{2})^{\frac{1}{3}} \quad (2.33)$$

Where a is the radius of the cylinder. The attenuation constant can be found as

$$\Omega_n^e = \frac{\alpha_n}{a} M e^{\frac{j\pi}{6}} \quad (2.34)$$

2.2.2.1. Gaussian Model

This model is a theoretical stochastic approach showing that received power variations can follow a Gaussian statistical model and that the loss is produced by a human when a person crossing the LOS can be present as a shape [29].

$$L(t) = -A_s \exp(-2((t - t_0)\frac{2}{T_s})^2) \quad (2.35)$$

Where A_s is the maximum loss, t_0 is the shadowing instant, T_s is the shadowing caused by a person crossing the LOS.

2.3. Comparison of the Models

Many comparisons between models have been made for accuracy. The METIS, Kirchhoff KED and GTD model, were compared with regard to accuracy of prediction of relative path loss in [11]. Loss produced by a human body at 11, 16, 28 and 32 GHz was investigated. The results show that the METIS model, Kirchhoff KED model and GTD model are able to simulate the human blockage effects well. In this study the DKED METIS model, which includes antenna gain is employed to predict the attenuation caused by human blockage(s), for the sake of simplicity and accuracy.

CHAPTER 3

RADIO PROPAGATION MODELING AND PRELIMINARY MEASUREMENTS

3.1. Radiation Propagation Modeling

Antennas are used to change the currents and voltage produced by the transmitted circuit into electromagnetic fields, which are propagated through space. In the nonexistence of material boundaries that affect waves, the field propagates as spherical waves, whose amplitudes change inversely with the distance from the antenna. The field strength and polarization can also be based on the direction of propagation. The antenna pattern function describes this variation, and it is one of the characteristics that identify different types of antenna. The other characteristic is the terminal impedance. Furthermore, these quantities and their dependence on the frequency are defined by the shape of the conductors and the dielectrics used to make the antenna. Figure 3.1 shows number of types of antenna.

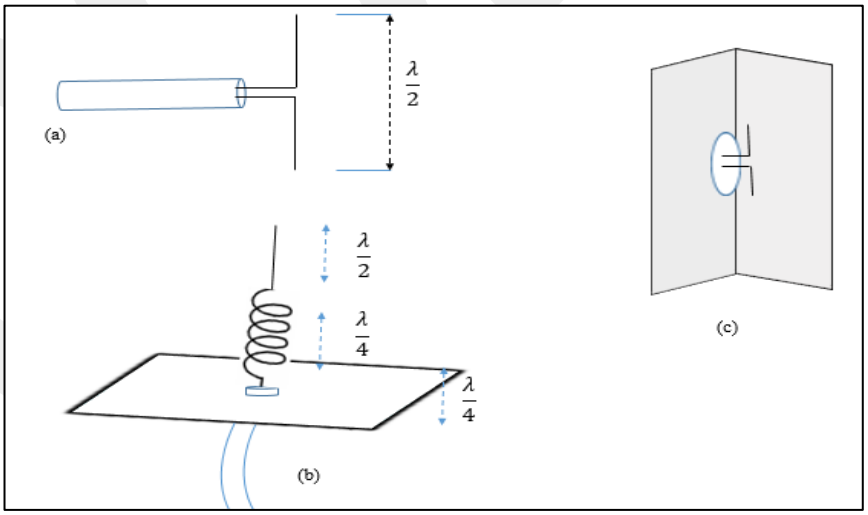

Figure 3.1. Simple antenna: (a) half wave dipole; (b) full monopole; (c) dipole with corner reflector.

This section has been compiled from [30]. From figure 3.2, the spherical radiation wave in the far field can be written as

$$E = a_E Z I \frac{e^{-jkr}}{r} f(\theta, \emptyset) \quad (3.1)$$

$$H = \frac{1}{\eta} a_r \times E \quad (3.2)$$

Referring to figure 3.2, r is the distance from the antenna, $k = {}^{2\pi}/_{\lambda}$ is the wavenumber, so the phase of kr is constant over spheres at the center of the antenna. a_e is unit vector, which describes the polarization of the electric field, which must be perpendicular to the unit vector a_r which is indicated to the radial direction away from the antenna, so the E tangent the spheres of constant phase. The magnetic field H is perpendicular to both E and a_e. The amplitude difference between E and H is $\eta = 377$, which is the wave impedance. Equation (3.1), I is the current of the terminal, Z is the impedance and $f(\theta, \emptyset)$ describes the direction of the fields and their variation.

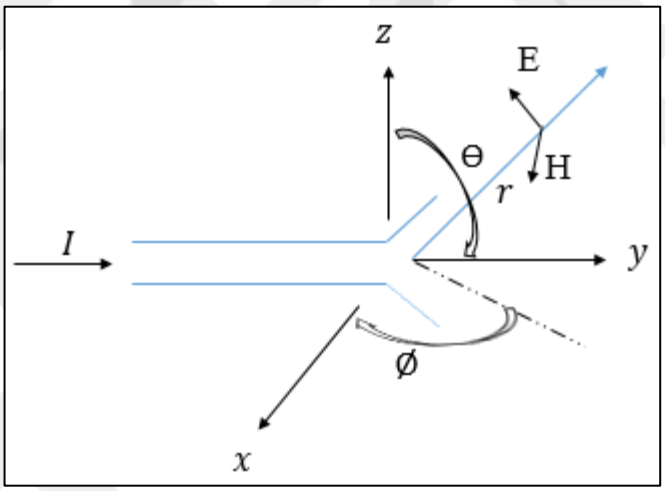

Figure 3.2. Spherical radiation into space by an antenna.

A greater number of studies have been conducted on the antenna regarding their radiation characteristics more than those of detectors, when used to receive signals, antennas have the same properties as when being used to transmission. In figure 3.3, there are two antennas, each having the terminal current and voltage as indicated. The antenna may be in free space or there may be objects around them. Since Maxwell's equations are linear, the terminal voltage and current fulfill the following linear relations

$$V_1 = Z_{11}I_1 + Z_{12}I_2 \tag{3.3}$$

$$V_2 = Z_{21}I_1 + Z_{22}I_2 \tag{3.4}$$

Where V_1, I_1 are voltage and current source respectively of terminal 1. V_2, I_2 are the voltage and current source respectively of terminal 2. Z is the impedance.

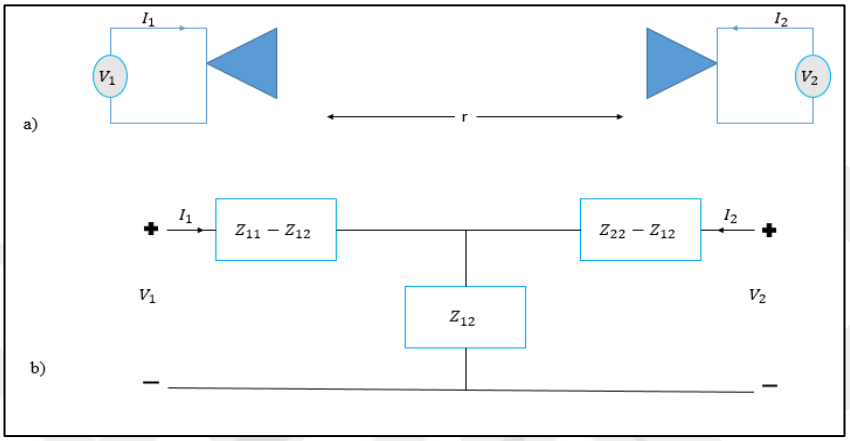

Figure 3.3. Pair of antennas for transmission and reception (a) with currents and voltages at the physical terminals of the antennas; (b) equivalent circuit.

When an environment around the antennas already includes ordinary dielectrics and conductor objects, the reciprocity relation implies that $Z_{12} = Z_{21}$. Furthermore, the antenna's terminal 1 is driven by current source I_1 and the antenna's terminal 2 is left open. The power delivered P_t to the antenna terminal is

$$P_T = \frac{1}{2}\, Re\{V_1 I_1^*\} = \frac{1}{2}\, Re\{Z_{11}|I_1|^2\} \tag{3.5}$$

With there is no loss of the antenna; this power is radiated into the space, then $Re\{Z_{11}\}$ must be radiation resistance R_{r1} of antenna 1, and $Im\,\{Z_{11}\}$ is terminal reactance X_1 of the antenna. The same process can be applied to antenna 2 for the same reasons.

$$\mathrm{Z_{11}} = \mathrm{R_{r1}} + \mathrm{jX_1} \tag{3.6}$$

$$\mathrm{Z_{22}} = \mathrm{R_{r2}} + \mathrm{jX_2} \tag{3.7}$$

For some frequencies the radiation and terminal reactances of an antenna are constant quantities, independent of the radial separation r among the antenna on condition that $r \gg \lambda$. If the terminal of antenna 2 is left open, the voltage V_2 will be proportionate to the electric field radiated by antenna 1, which is located at distance r. Therefore, the ratio $Z_{12} = V_2/I_1$ will decrease with the distance, then Z_{12} becomes much smaller than $|Z_{11}|$ or $|Z_{22}|$.

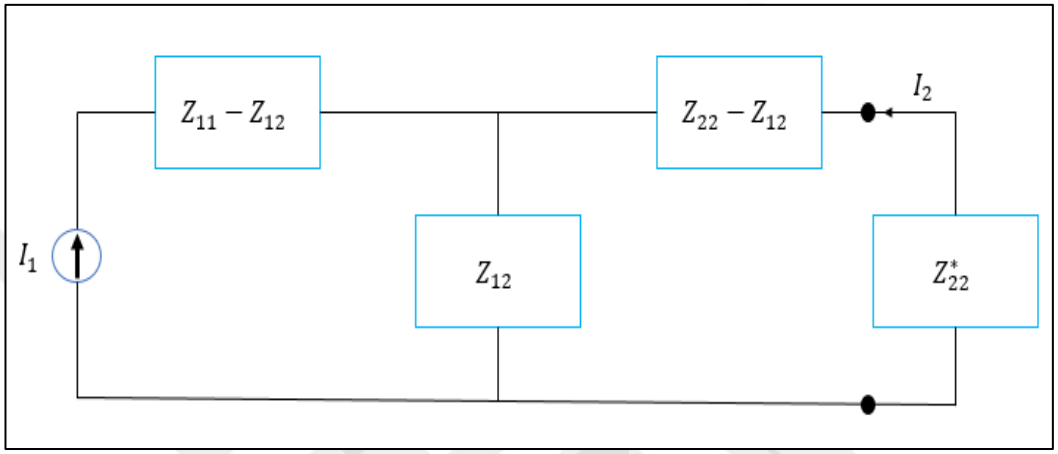

Figure 3.4. Equivalent circuit for a pair of antennas, which a current source applied to antenna 1 and conjugate matched load connected to antenna 2.

Now suppose terminals of antenna 2 is connect to a conjugate load Z_{22}^* as explained in figure 3.4. It is clearly shown that I_2 is given by

$$\mathrm{I_2} = -\mathrm{I_1}\frac{\mathrm{Z_{12}}}{(\mathrm{Z_{22}} - \mathrm{Z_{12}} + \mathrm{Z_{22}^*}) + \mathrm{Z_{12}}} = -\mathrm{I_1}\frac{\mathrm{Z_{12}}}{2\mathrm{R_{r2}}} \tag{3.8}$$

Therefore the received power by resistance R_{r2} is given by

$$\mathrm{P_R} = \frac{1}{2}\mathrm{R_{r2}}|\mathrm{I_2}|^2 = \frac{1}{8}\frac{|\mathrm{Z_{12}}|^2}{\mathrm{R_{r2}}}|\mathrm{I_1}|^2 \tag{3.9}$$

With the conditions of conjugate matching load in figure 3.4, the delivered power by I_1 is

$$\mathrm{P_T} = \frac{1}{2}|\mathrm{I_1}|^2\mathrm{Re}\left\{(\mathrm{Z_{11}} - \mathrm{Z_{12}}) + \frac{(2\mathrm{R_{r2}} - \mathrm{Z_{12}})\mathrm{Z_{12}}}{(2\mathrm{R_{r2}} - \mathrm{z_{12}}) + \mathrm{Z_{12}}}\right\} = \frac{1}{2}|\mathrm{I_1}|^2\frac{2\mathrm{R_{r1}}\mathrm{R_{r2}} - \mathrm{Re}\{\mathrm{R_{12}^2}\}}{2\mathrm{R_{r2}}} \tag{3.10}$$

It is common to define the path gain PG as the ratio of the received power P_R to the transmitted power P_T, and its inverse is the path loss PL. Since $P_R < P_T$ the PG is less than unity and the path loss is greater than unity. From (3.9) and (3.10) PG can be written as

$$\mathrm{PG} = \frac{\mathrm{P_R}}{\mathrm{P_T}} = \frac{|\mathrm{Z_{12}}|^2}{4\mathrm{R_{r2}R_{r1}} - 2\mathrm{Re}\{\mathrm{Z_{12}^2}\}} \tag{3.11}$$

In the same context, the antenna may have an effective area $\mathrm{A_e}$ with unit m^2. The received power is product of the $\mathrm{A_e}$ and incident power densityin W/m^2. If antenna 1 is a transmitter, as shown in figure 3.5a, and the antennas have the same polarization then

$$\mathrm{P_R} = |\mathrm{P}|\mathrm{A_{e2}} = \mathrm{P_T}\frac{\mathrm{g_1}(\theta,\emptyset)}{4\pi\mathrm{r}^2}\mathrm{A_{e2}} \tag{3.12}$$

Where P is the power density, $\mathrm{A_{e2}}$ the effective area of antenna 2, $\mathrm{g_1}$ is the gain of antenna 1 and the direction of the gain dependence on $(\theta, \emptyset)$.

If antenna 2 is the transmitter as shown in figure 3.5b, and the antennas have the same polarization then

$$\mathrm{P_R} = |\mathrm{P}|\mathrm{A_{e1}} = \mathrm{P_T}\frac{\mathrm{g_2}(\theta,\emptyset)}{4\pi\mathrm{r}^2}\mathrm{A_{e1}} \tag{3.13}$$

Where $\mathrm{A_{e1}}$ is the effective area of antenna 1, and $\mathrm{g_2}$ is the gain of antenna 2.

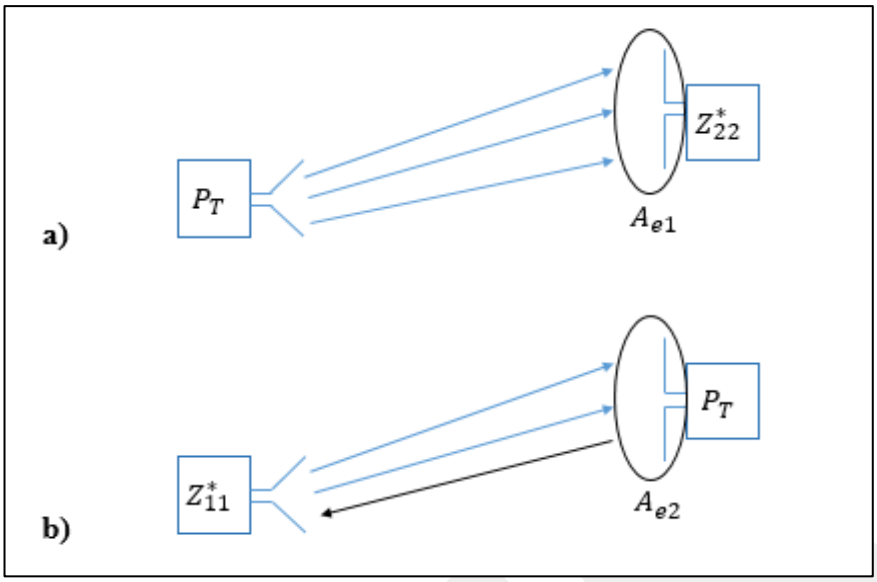

Figure 3.5. Effective area of the receiving antenna, (a) antenna 1 transmits power; (b) antenna 2 transmits power.

Hence it appears from (3.12) and (3.13) that

$$g_1 A_{e2} = g_2 A_{e1} \quad \text{or} \quad \frac{A_{e1}}{g_1} = \frac{A_{e2}}{g_2} \tag{3.14}$$

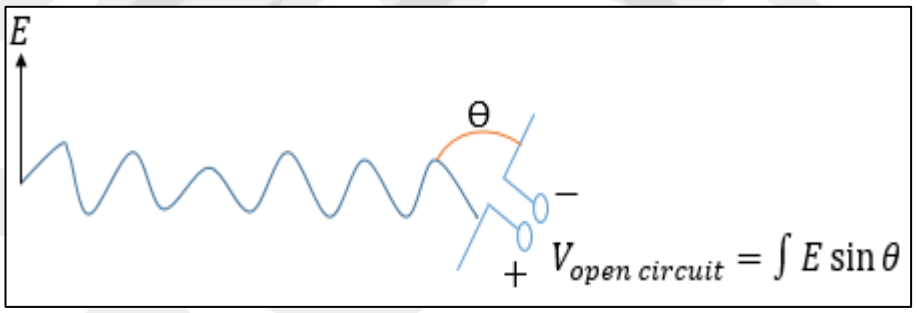

Figure 3.6. Hertzian dipole acting as a receiver of an indirectly arriving wave.

In figure 3.6 the antenna integrates the electric feild component along its axis. Consequently the open circuit voltage V_{oc} (voltage crosses conjugate load Z_{22}^* in figure 3.4) is given by

$$V_{oc} = \int |E| \sin\theta \tag{3.15}$$

Where E is is the components of incident feild of the plane of incidence. Therefore, recalling the relastion between the electric field E and an magnatic field H in terms of A_e for the Hertzian dipole, it is found that

$$\frac{A_e}{g} = \frac{\lambda^2}{4\pi} \tag{3.16}$$

Consequently using the expression in (3.12) and (3.13), it be seen that the path gain PG for the antenna in free space is given by

$$PG = g_1 g_2 \left(\frac{\lambda}{4\pi r}\right)^2 \tag{3.17}$$

The path gain PG is the ratio of the received power P_R and transmitted power P_T, and its inverse is the path loss PL. The path loss in free space $FSPL$ when the g is unity, is given by

$$FSPL = \frac{P_t}{P_r} = \frac{(4\pi d)^2}{\lambda^2} = \frac{(4\pi fd)^2}{c^2} \tag{3.18}$$

Moreover, the path loss is a main component in the analysis and design of the link budget of wireless communication systems. The transmission loss in indoor environment is very high. Especially at millimeter wave frequencies, because of their short wavelength. The next stage includes an experimental study on the effects of human body movement on an indoor environment at 18 – 22 GHz. This is a part of the continuing research of this study.

3.2. Preliminary Measurements

The purpose of the experimental is to determine the effects of human body movement on the indoor radio wave propagation at 18 – 22 GHz. It is a part of continuing research that studies human body blockage in short range indoor links at 28 – 30 GHz.

The measurement system is VNA based and it includes a transmitter (Tx) and receiver (Rx) directional antennas, a Vector Network Analyzer (VNA), and a controlling computer as shown in figure 3.7.

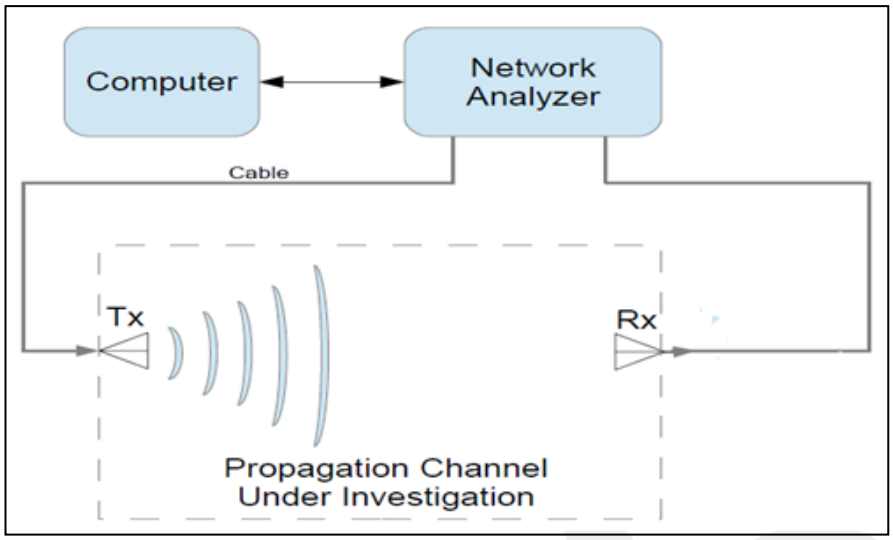

Figure 3.7. Measurement system.

In the measurement system, two horn antennas (ARRA Inc.) are used. The antennas are connected to the VNA (Agilent E8363A) that communicates with a notebook computer for signal analysis. The horn antennas connected to the VNA have a minimum gain of 15dBi and a maximum gain of 18dBi. Low loss cables are used for such connections. Both antennas are placed on a stand with a height of 0.5m .Data analysis is performed in MATLAB. All measurements are carried out at RF and Antenna laboratory of Electrical and Electronics Engineering department of Atilim University. Simply, the frequency-domain channel sounding method is proven for indoor link, it has been selected for 18 – 22 GHz band. An oscilloscope or a signal generator is not needed to set up the system at this stage. However, calibration measurements is required. The VNA, SOLT (Short, Open, Load and Thru) type of calibration is used. This type is based on short, open, load and thru standards. It is widely used as a type of calibration that eliminates systematic error terms. Figure 3.8 shows the result of calibration when the terminals of the VNA are directly connected. In addition, this is an easy and suitable approach for different kinds of environments, and it is commonly used in coaxial measurements.

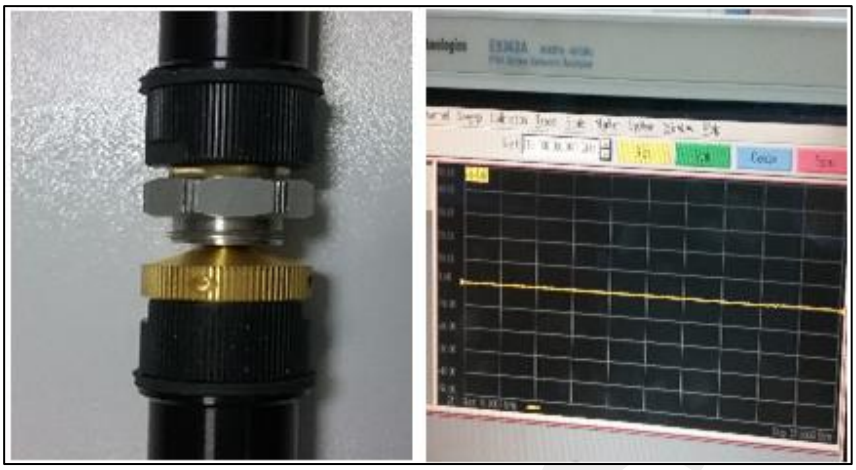

Figure 3.8. VNA calibration result.

Moreover, the calculation of loss due to connectors and cables are required to make accurate calibration as shown in figure 4.9, in addition to the path loss for the measurement system. Such calculations are made with the use of the following equation (here, shadowing is neglected)

$$P_r = P_t + G_t + G_r - L_{Total} \quad dB \tag{3.19}$$

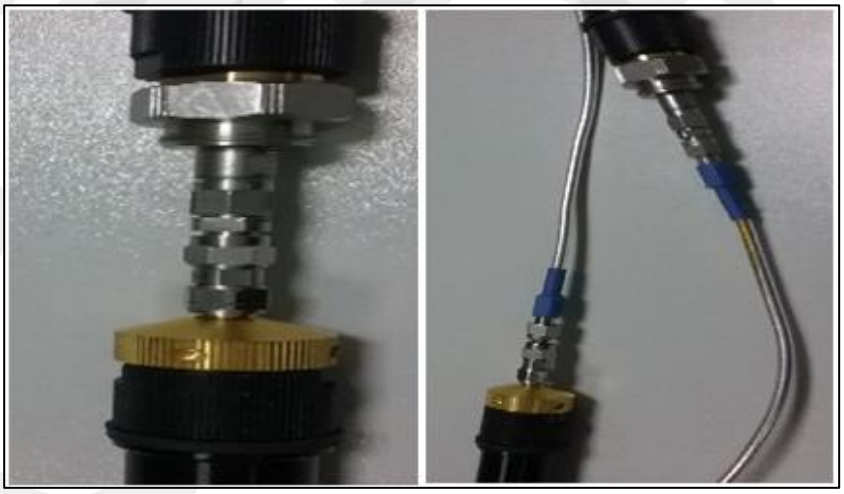

Figure 3.9. Measurement of the power loss due to used connectors and cables.

Where P_t is transmitted power, G_t is the transmit antenna gain, G_r is the receive antenna gain, and L_{Total} is the total loss which corresponds to

$$L_{Total} = P_L + L_C \quad dB \tag{3.20}$$

Where L_C is the total loss of cable and connector, and P_L is the path loss which can be calculated as [18].

$$P_L = -147.5522 + 20\log_{10}(f) + 20\log_{10}(d) \text{ dB} \quad (3.21)$$

Where f is the frequency, and d is the distance between the transmitter and the receiver. The measurement setup in the laboratory environment is shown in Figure 3.10. For the purpose of VNA calibration, d was decided to be 2.5 m.

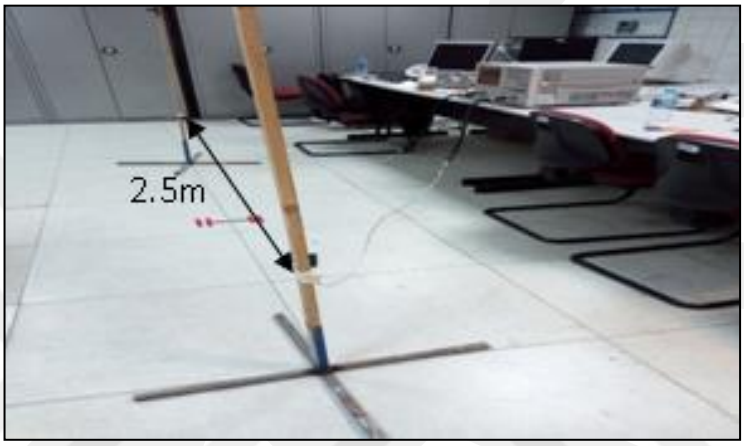

Figure 3.10. Measurement setup.

To ensure proper calibration, results from comparing calculated received power (P_r) and measured received power as a function of frequency ($G(f)$) for free space case are obtained. As shown in Figure 3.11, it is clear that the $G(f)$ matches the calculated received power $P_r(f)$ or P_r. Thus, the accuracy of further measurements is highly expected [18].

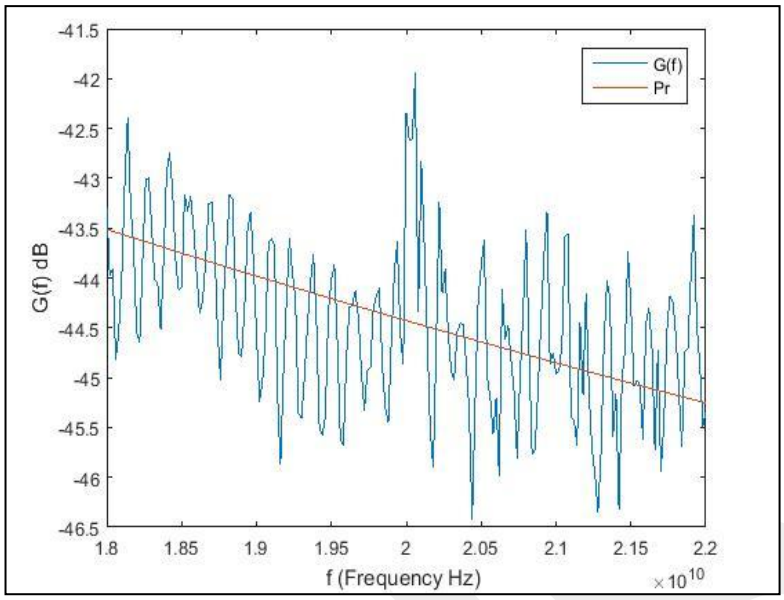

Figure 3.11. Signal variation for P_r(f) and $G(f)$ after calibration.

In order to find out the effect of human body movement on the channel in the indoor environment, three different scenarios are chosen. In each scenario, the distance between the transmitter and the receiver (d) is set at 2.5m. In the scenarios, the radio link at 18 – 22 GHz is blocked by a human body in two different states: first, full blockage state where the human body is positioned at the center of LOS ink. Second, partial blockage where the human body is moved to left and right from the center position by 6 cm. The measurement setup of full blockage state is illustrated in Figure 3.12.

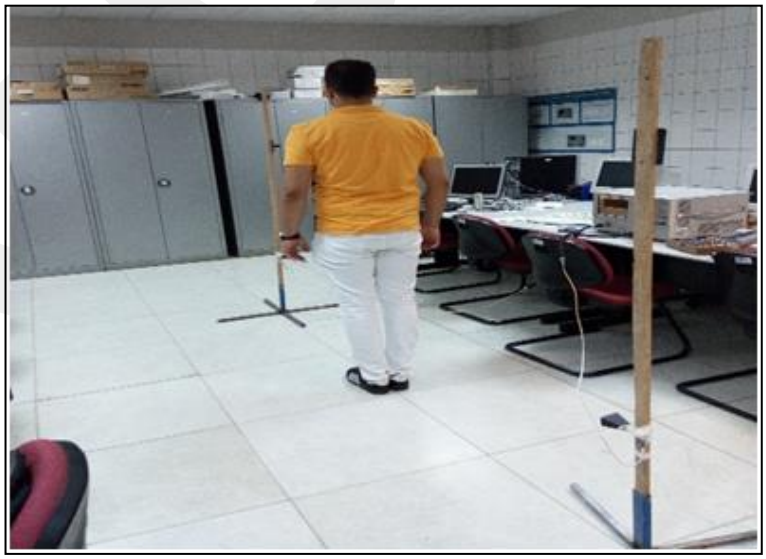

Figure 3.12. Radio link fully blocked by a person.

Table 3.1. Scenarios of measurement details.

Scenario #	Blockage Case	Position
1	Full	Center
2	Partial	6cm left
3	Partial	6cm right

Measurement results for scenario 1 are presented in Figure 3.13. When the results are compared with the free space case shown in Figure 3.11, the effect of human blockage can be easily noticed.

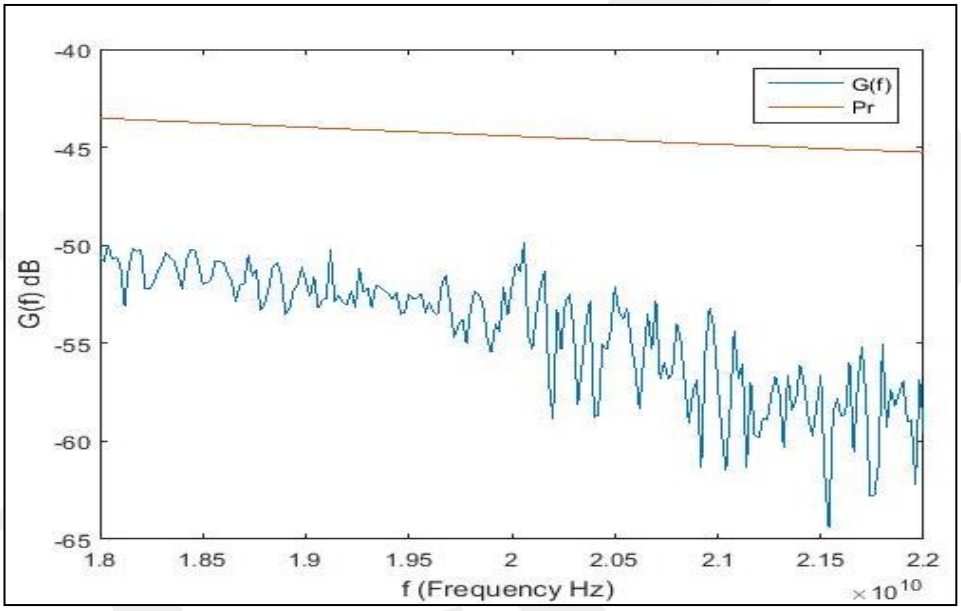

Figure 3.13. Signal variation for free space and human body blocked link.

Additionally, measurement results for scenario 2 is illustrated in Figure 3.14, while Figure 3.15 shows measurement results for scenario 3. It is noted that at minimum blockage, $G(f)$ tend to approach the P_r, as predicted. However, degradation on the received signal power is observed despite a little movement on the link. Similar degradation levels are obtained for both scenarios.

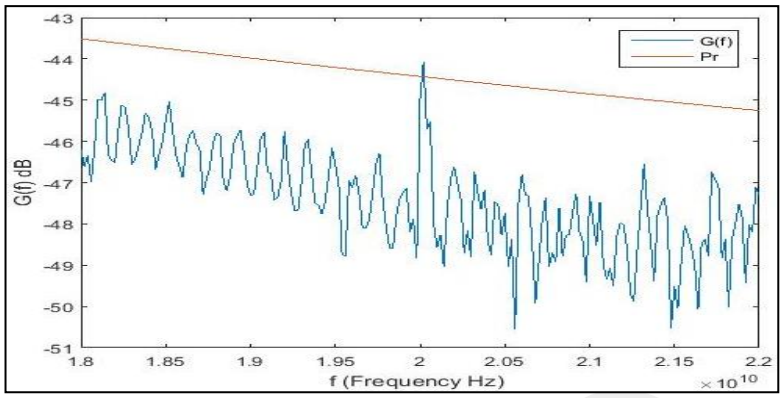

Figure 3.14. Signal variation for free space and human body partially blocked link from the left.

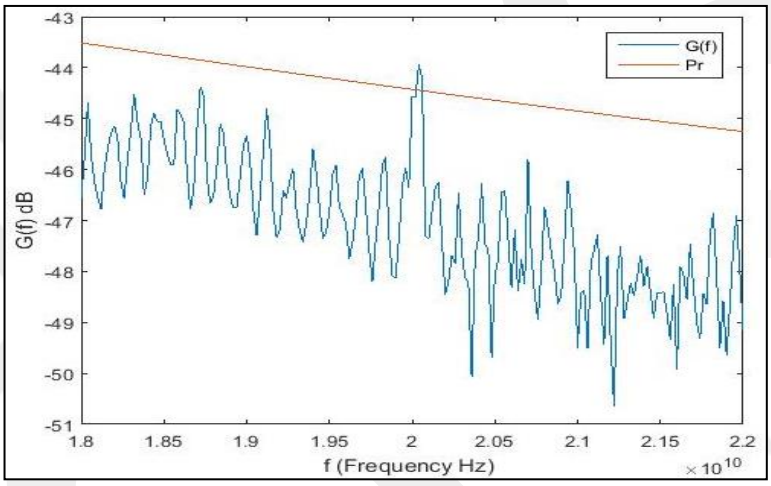

Figure 3.15. Signal variation for free space and human body partially blocked link from the right.

Based on the measurement results, it is obvious that the human body movement on the link caused a variation of received signal power levels. In addition, the measured received signal power levels for both movement cases are at the same level, which proves that the calibration process is successfully performed for the selected frequency range despite its difficulty at such range. And surely, such results will inspire us to study the effects of local objects close to the indoor link on the directional propagation in millimetre wave bands (28 – 33 GHz). However, any increase in the measurement receiver band is offset by an increase in its noise level. Therefore, the noise level must be determined.

The noise floor of the received radio signal consisted of different noise sources, which may have included thermal noise, atmospheric noise and noise from components of the measurement system. It is the lowest possible signal level that the system can

measure, as shown in figure 3.16. In this study, when the frequency band are increase to 28:30 GHz, the noise level is determined by the measurements.

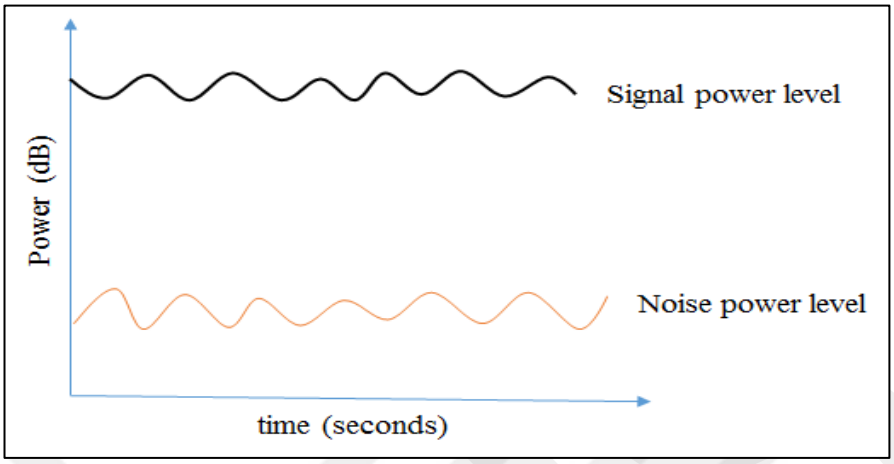

Figure 3.16. Received signal power level to the noise power level ratio.

It is an important process to determine whether the current system is appropriate to measure millimetre wave bands (28 – 33GHz). To do so, the measurement setup in the laboratory environment, as shown in the figure 3.10. The received power in free space is measured. The LOS is blocked by a person at the center (1 meter away from the transmitter), as shown in the figure 3.12. Then the received measurement power is measured, as in figure 3.17.

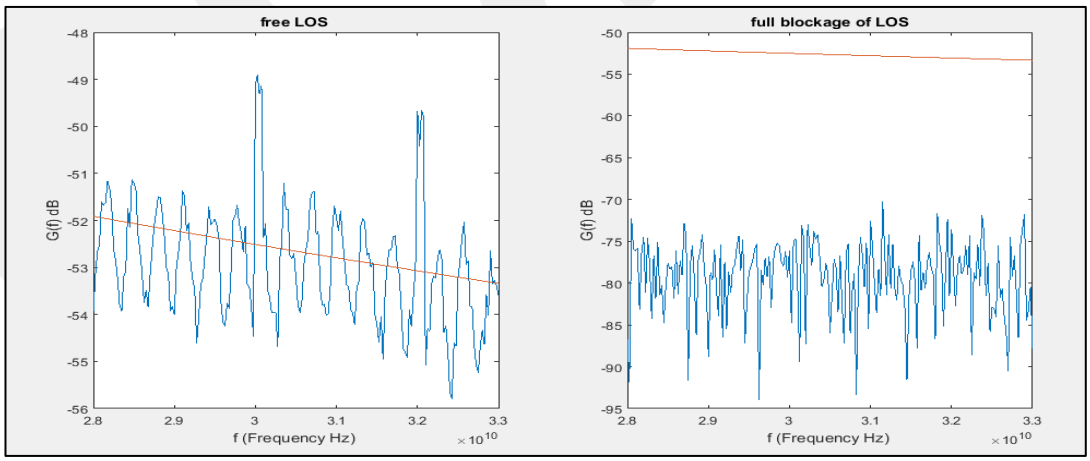

Figure 3.17. The received measurement power at free space LOS and full blockage LOS.

To find out whether the received signal would combine with the noise floor, the person is replaced by a plate of metal. Subsequently, the LOS is blocked by the plate of metal

at the center (1 meter away from the transmitter), as shown in figure 3.17. Then the received measurement power is measured. The plate is moved to 1.25 meters as well as 1.5 and 2 meters. The received power is measured at each movement, as shown in figure 3.18.

Figure 3.18. Full blockage LOS at center by plate of metal.

The results show that the noise floor determined, as shown in figure 3.19. The signal was blocked by a person very close to the noise floor, and there is no guarantee to be determined in different scenarios.

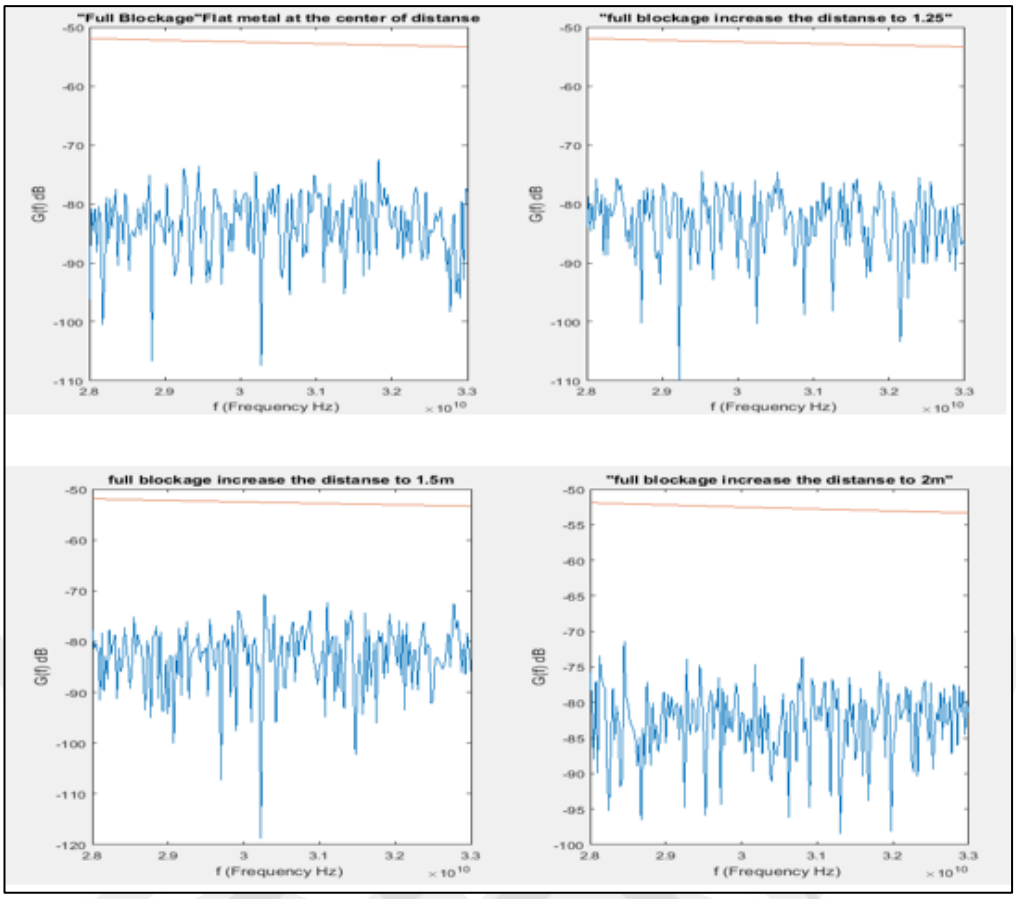

Figure 3.19. The received power measurements of NLOS.

Examining the noise floor by using a spectrum analyzer (E4448A 3Hz-50GHz), and a signal generator (E8244A 250KHz-40GHz) instead of VNA. The same antennas, environment, cables and connectors are used as shown in Figure 3.20.

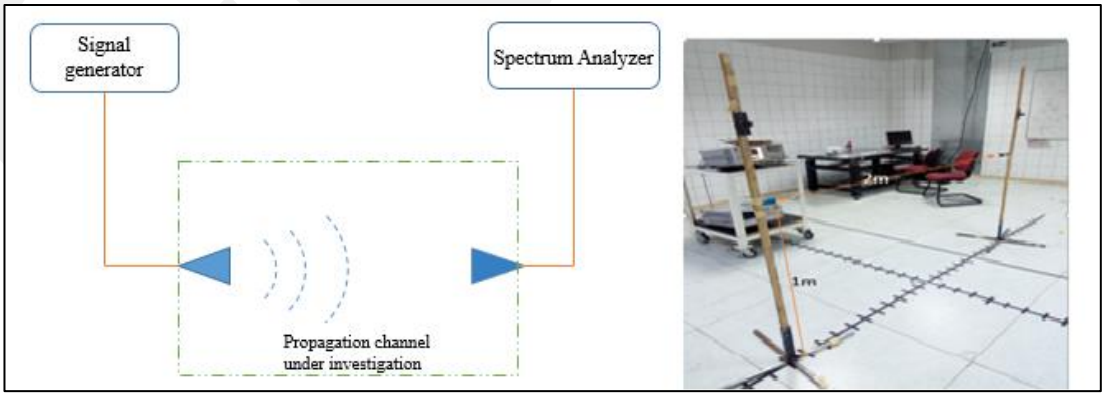

Figure 3.20. Measurement setup.

The spectrum analyzer as well as the signal generator are prepared to receive and transmit 28GHz to 33GHz signals respectively, each with 2.4 KHz bandwidth. The

LOS received power in free space and a fully blocked link by a human body are measured as shown in figures 3.21, 3.22, 3.23 and 3.24. The results of the measurements show that the signal strength in the free space LOS as well as in the full blockage LOS is sufficiently far from the noise floor. Thus, the current system is appropriate to measure the effects of scattering objects around indoor links in the millimetre wave band (28 – 33 GHz).

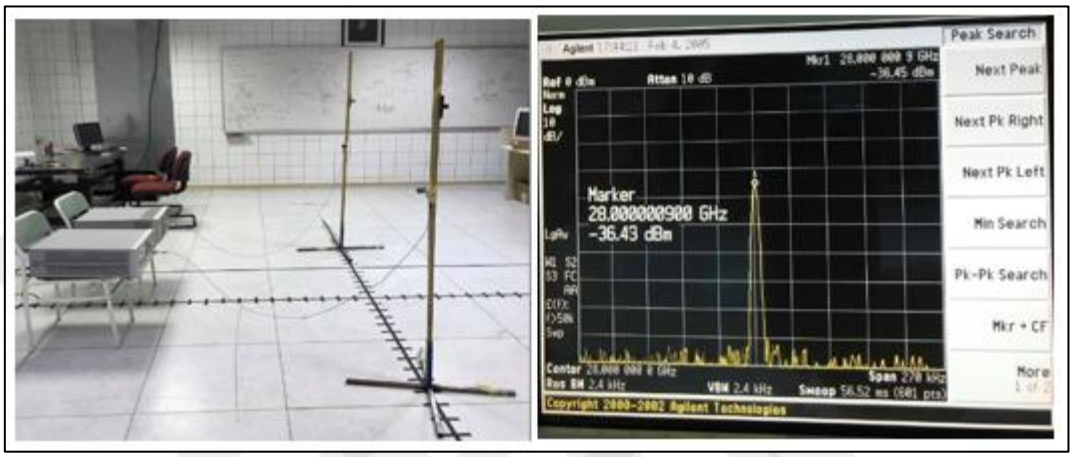

Figure 3.21. Free space measurements at 28 GHz.

Figure 3.22. Full blockage link measurements at 28 GHz.

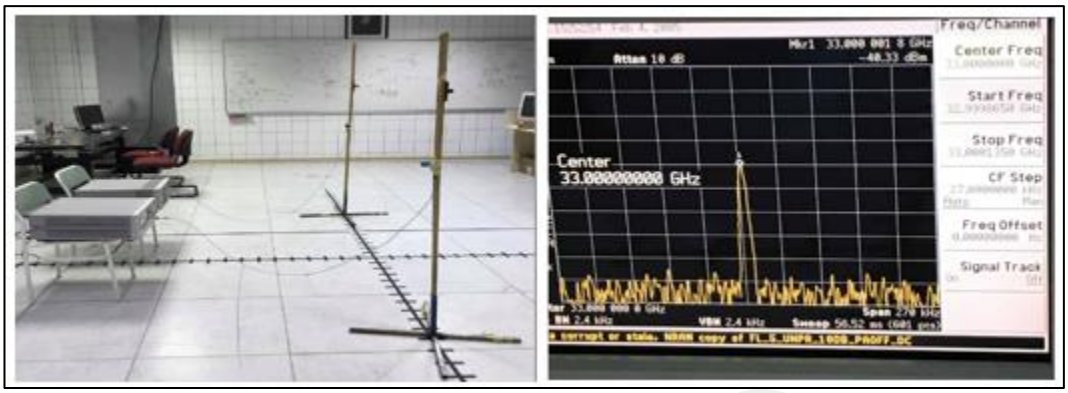

Figure 3.23. Free space measurements at 33 GHz.

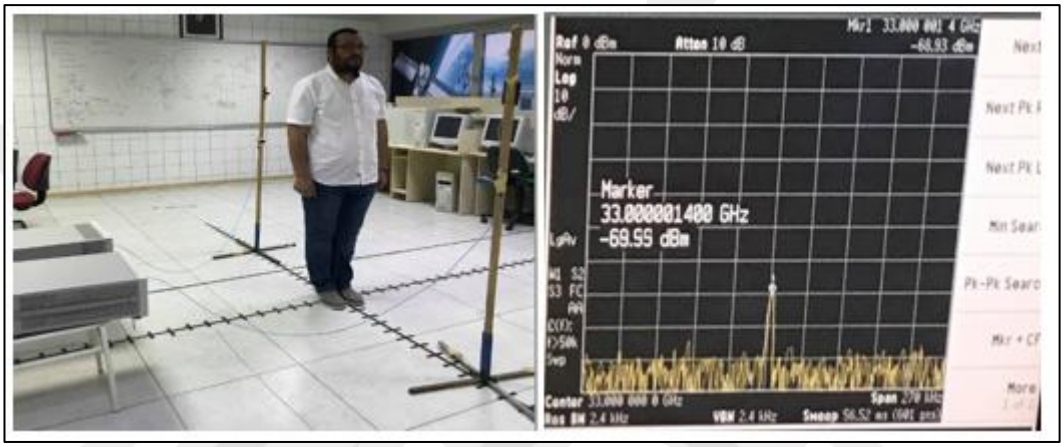

Figure 3.24. Full blockage link Measurement signal at 33 GHz.

CHAPTER 4

MODELING OF HUMAN BODY SHADOWING AND NEARBY OBJECTS

This stage presents a simple approach to characterize the effects of scattering objects around indoor links at 28 GHz while the link is fully blocked by human body. In the study, two scattering objects, a metallic reflector and a human body, are considered. To do this, simple propagation models such as reflection and diffraction are incorporated. In the diffraction modelling, for the sake of simplicity, the DKED model is employed to predict the attenuation caused by human blockage(s). In the reflection modelling, specular reflection model is used to predict the attenuation due to metallic reflector. The accuracy of the models are then evaluated by comparing the simulations with the measured received powers.

4.1. Measurement Setup and Environment

As illustrated in Figure 4.1 ,the measurement system includes a transmitting antenna (Tx), a receiving antenna (Rx), a spectrum analyzer, and a signal generator .For transmitting and receiving, two horn antennas (PE9850/2F-20) with 18.3^0 horizontal and 16.7^0 vertical half-power beamwidth (HPBW) and 20 dBi of gain are used. These antennas are positioned on a stand with 1 m high, and a distance of 2 m is kept between the antennas. While the Tx is connected to Agilent E8244A signal generator, the Rx is connected to Agilent E4448A spectrum analyzer. Low loss cables are used for such connections.

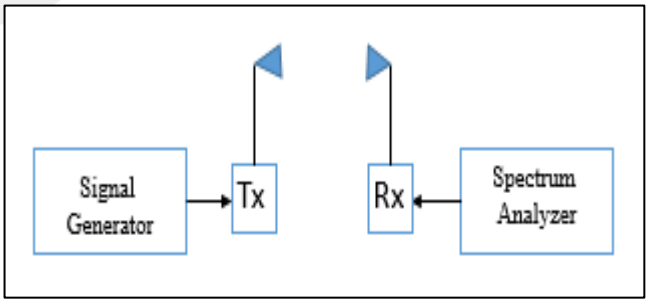

Figure 4.1. Measurement system.

To ensure perfect measurement conditions, pre measurement procedure is carried out. Here, an indoor propagation link is created. The link is aligned to human body with the use of a laser beam. In addition, the loss due to connectors and cables is measured, and preliminary measurements are done to calibrate the system.

The measurements are performed at RF and Antenna laboratory of Atilim University. The laboratory environment layout is shown in Figure 4.2, where the link is placed between a wall and a desk with a height of 0.75 m. The distance from both the wall and the desk to the link is $L_1 = L_2 = 2.4$ m. Steel cabinets with a height of 2.2 m are located behind Tx . These steel cabinets are $L_3 = 13.5$ m away from the Tx. Behind the Rx, there is a plaster board on a wall. This is $L_4 = 3$ m away from the Rx. The ceiling height of the laboratory room is 2.9 m. In addition, the impacts of multipath from the fixed scatters are studied as follow. First, the link is presumed to be blocked by a human body with 0.5 m body width. It is regarded that signals radiated from Tx are diffracted from point 1 (shoulder of the human body). Then, the positions of the scatters that are contributing to the received power are determined (2, 3, and 4). Next, the received power resulted from these scatters and from human body are calculated. Furthermore, the difference (isolation) between the received power of the human body and multipath components is found. From the results, 14 dB isolation is obtained. Consequently, multipath powers from the fixed scatters can be neglected.

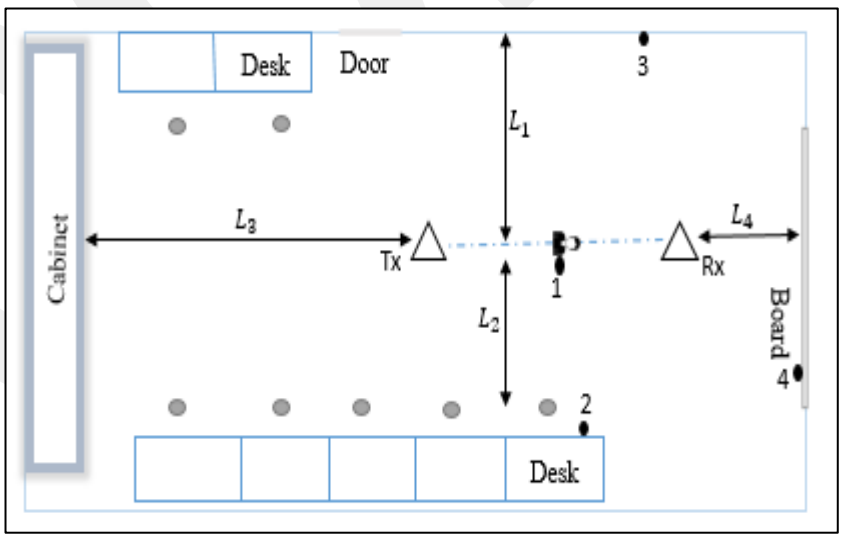

Figure 4.2. Floor plan of the laboratory environment.

Measurements are repeated three times at each position of the blocker in order to obtain stable measurement system, and the mean value is taken. Recordings of the received

signal power are made on perpendicular polarization. Measurement cases performed in this study are described in the following.

4.2. Scenarios

In this section, the two scenarios are don. The first the propagation link is blocked by a person with a body width of 0.5m, while a metallic reflector approaching towards the link, as shown in Figure 4.3 (a). The second the same person blocking the link while another person with a body width of 0.47m approaching the link, as shown in Figure 4.3 (b).

4.2.1. Scenario I - Human Body Blocking the Link While a Reflector Approaching Towards the Link

As in figure 4.3 (a), the metallic reflector is placed on a stand with 1 m high. The reflector has dimensions of 1 m (width) × 1 m (length) × 1 mm (thickness). During the measurements, the reflector is moved from -1 m to -0.3 m. Here, movement is limited to -0.3 m owing to the body width of the person in order to avoid overlapping of the blockers. At every 10 cm step, the received power is measured from 8 positions.

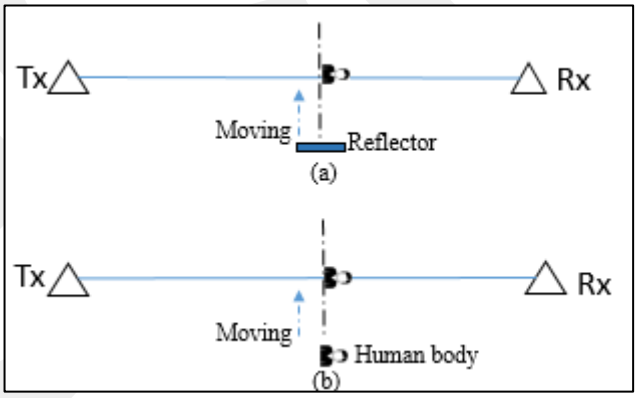

Figure 4.3. Measurement scenarios: a) Scenario I, b) Scenario II.

4.2.2. Scenario II - Human Body Blocking the Link While Another Human Body Approaching Towards the Link

In this case a person with a body width of 0.5m blocks the link, while another person with a body width of 0.47m approaching the link as shown in Figure 4.3 (b). Through

the measurements, the person approaching the link is moved from -1 m to -0.6 m so that overlapping of the blockers can be avoided. The measurement of received power is taken at every 10 cm step from 5 positions.

4.3. Modeling of Scattering Objects While Human Body Blocking the Link

This part presents a brief description of the models suggested for each measurement case. DKED model [10] for the purpose of predicting the attenuation caused by human blockage.

Among the several accurate methods that have been suggested in the study, DKED is selected due to its simplicity in simulating the human blockage as well as its efficiency in reducing the complexity of the modelling of multiple human blockers. In DKED model, human blockage is estimated using a rectangular screen with infinite vertical height. Only the side edges of the screen are considered for diffraction. The top-down projection of the blockage is shown in Figure 4.4. The shadowing loss of the blockage is then given in decibels by

$$SL = -20\log_{10}\left|\left(\frac{1}{2} - F_{w1}\right) \times \sqrt{G_{Txw1}(\theta)} \times \sqrt{G_{Txw2}(\theta)} + \left(\frac{1}{2} - F_{w2}\right) \times \sqrt{G_{Rxw1}(\theta)} \times \sqrt{G_{Rxw2}(\theta)}\right| \quad (4.1)$$

The corresponding shadowing incurred by each of the two edges (w1and w2) is based on KED and is determined by

$$F_{\mathrm{w1,w2}} = \frac{\tan^{-1}(\bar{+}\sqrt{\frac{\pi}{\lambda}((\mathrm{D_{2w1,w2}} + \mathrm{D_{1w1,w2}}) - \mathrm{r})})}{\pi} \quad (4.2)$$

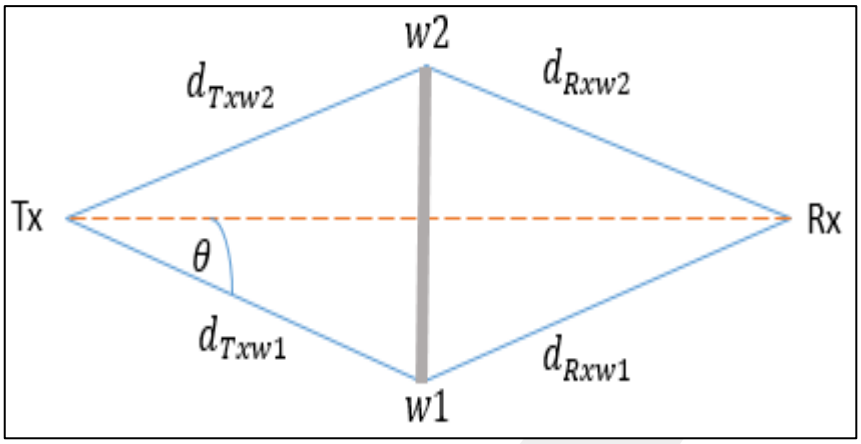

Figure 4.4. Top-down projection of the blockage.

To prove how appropriate the DKED model is , the received power is measured with a person crossing the link between the Tx and the Rx as in the procedure in [9] and shown in figure 4.5. It is found that the attenuation resulting from the human blockage matches the DKED model

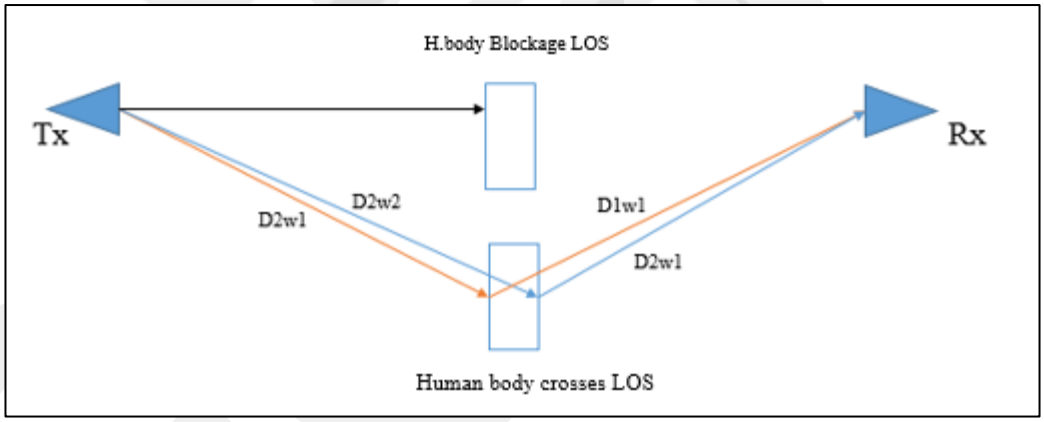

Figure 4.5. DKED geometry for the signal of the person crossing the link.

However, in Case I, in addition to a human blockage, there is a metallic reflector which causes specular reflections. An illustration of the proposed model in this case is shown in Figure 4.3 (a). By using a specular reflection model along with the DKED model, the received power can be calculated as [31].

$$P_r = P_t + G_{TxP}(\phi) + G_{RxP}(\phi) - PL \tag{4.3}$$

Where P_r is the received power, P_t is the transmitted power, ϕ is the projected angle from the Tx to the center of the metallic reflector (C) and from C to the Rx, $G_{Tx|Rx}(\phi)$

are the normalized gains of the antennas relative to boresight gain, and PL is the total loss. When studying the total loss characteristics, reflection and diffraction should be considered. Evidently, propagation from the Tx to the Rx is considered to be reflection happening at the center of the metallic reflector along with the diffraction occurring over the sides of the blocker on the link. With this consideration, the PL is the product of: 1) the reduction in the field due to diffraction of the human body blocking the link (PL_1), and 2) the reduction in the field due to reflection from the reflector approaching towards the link (PL_2). Thus, the path loss expressed in decibels is [30]:

$$PL = PL_1 + PL_2 \tag{4.4}$$

In (4.4), PL_1 is the product of two components: the free-space path loss (2) and SL that is found in equation (4.1).

$$PL_0 = 20\log_{10}[(\lambda/4\pi r)] \tag{4.5}$$

where λ is the carrier wavelength. Similarly, PL_2 is the product of two components: PL_0, and the loss due to reflection (|Γ|) [32]. The dielectric properties of the metallic reflector and angle of incident effect on its reflection coefficient ($\Gamma_{\perp\parallel}$) are shown in figure 4.6.

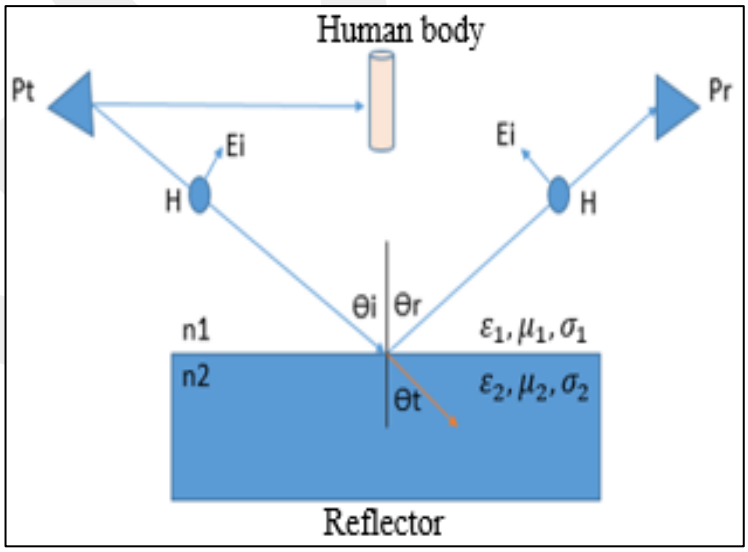

Figure 4.6. Reflection and transmission signal at the surface on the plane of incidence.

Where i, r, t indicate the incident, reflected, and transmitted fields, respectively, and $\varepsilon_i, \mu_i, \sigma_i$ are indicate to the permittivity, permeability, and conductivity of the two media. The reflection coefficient of the metallic reflector can be calculated based on equations (4.6) and (4.11). The result is shown in figure 4.7.

$$E_r = \Gamma_\perp * E_i \tag{4.6}$$

$$E_r = \Gamma_\parallel * E_i \tag{4.7}$$

$$\theta_i = \theta_t \tag{4.8}$$

$$\Gamma_\perp = \frac{\cos\theta_i - \sqrt{\varepsilon'' - \sin^2\theta_i}}{\cos\theta_i + \sqrt{\varepsilon'' - \sin^2\theta_i}} \tag{4.9}$$

$$\Gamma_\parallel = \frac{-\varepsilon'' * \cos\theta_i - \sqrt{\varepsilon^* - \sin^2\theta_i}}{\varepsilon'' * \cos\theta_i + \sqrt{\varepsilon^* - \sin^2\theta_i}} \tag{4.10}$$

$$\varepsilon'' = \frac{\sigma}{2\pi f \varepsilon_0} \tag{4.11}$$

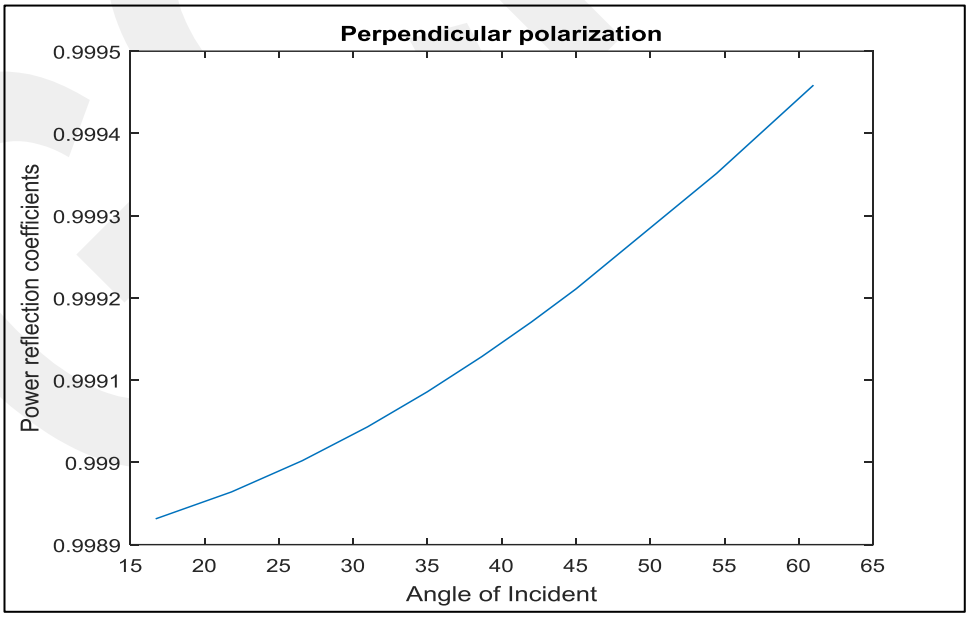

Figure 4.7. The reflection coefficient of the metallic reflector.

For this case, r in PL_0 is the total distance between the Tx to C and C to Rx. An illustrative example of the propagation model of Scenario II is shown in Figure 4.8 (b). In this propagation model, only the diffraction mechanism is considered. It is worth noting that the reflection from human body could also be utilized. Clearly, this is burdensome and detracts from the primary focus of this study. Thus, both human bodies are modelled by using the DKED model as it provides an adequately accurate prediction of human body attenuation. However, the reflection could still be studied for scattering from the human body. To calculate the received power, it is essential to treat PL by means of revising PL_2 in equatipn (4.4). In this state, PL_2 is the product of PL_0 and SL_m where SL_m is the shadowing loss produced by the human body approaching towards the link, and can be calculated by using (4.2) and (4.1).

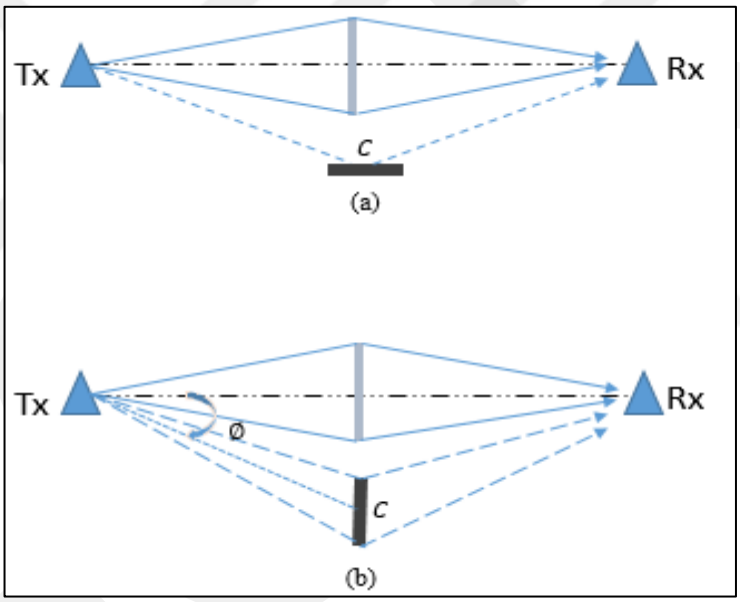

Figure 4.8. Propagation model (top-view): a) Scenario I, b) Scenario II.

4.4. Measurement Results

In order to evaluate the applicability of the models, the model simulations and the measurement results are compared for both scenarios.

Before performing the measurements, antenna gains (G_Tx|Rx (ϕ)) at each position of the reflector, are measured, as shown figure 4.9 and figure 4.10. The gain values are listed in Table 4.1 and compared with the radiation pattern of the antenna datasheet. The measured antenna gains are validated within a 2–10 dB error margin. It should be noted that there is still an ambiguity in the gains of the antennas.

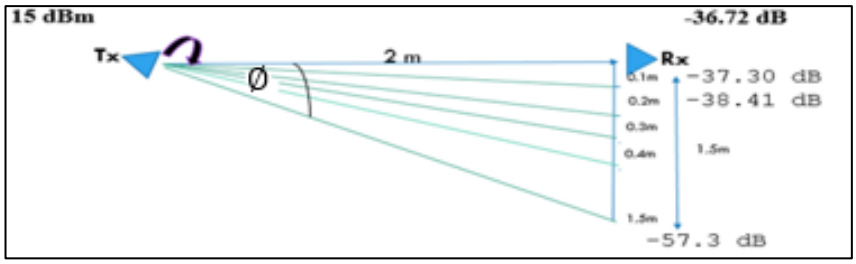

Figure 4.9. Measured gain at each step.

Table 4.1. Measurements of antenna gain based on Rx (ϕ).

Rx (ϕ)	G_Tx
2.86	19.29
5.71	18.71
8.53	17.6
11.30	16.11
14.03	14.41
16.69	12.31
19.29	10
21.80	8.51
24.22	5.71
26.56	4.11
28.81	3.11
30.96	2.51
33.02	1.11
34.99	0

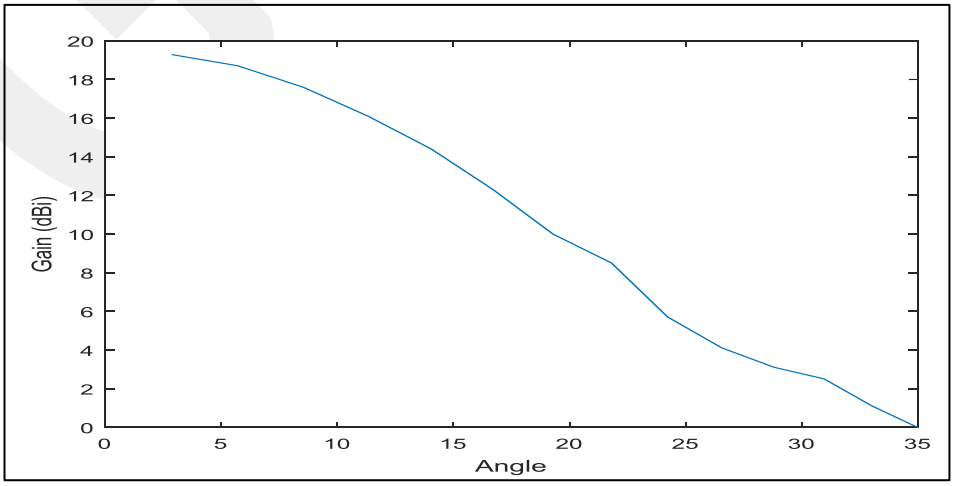

Figure 4.10. Antenna's beam based on its angle.

4.4.1. Scenario I

Figure 4.11 illustrates the comparison of the received power from the measurements and the model simulation. It can be noticed that at certain points where the metallic reflector is close to the propagation link (between -0.3 m and -0.5 m), the model exceeded the measured received powers by nearly 2 dB whereas at the other points, where the reflector is not close from the link, the model underestimated the measurements. It is notable that the blockage attenuation is significantly affected by the normalized gains of the antennas.

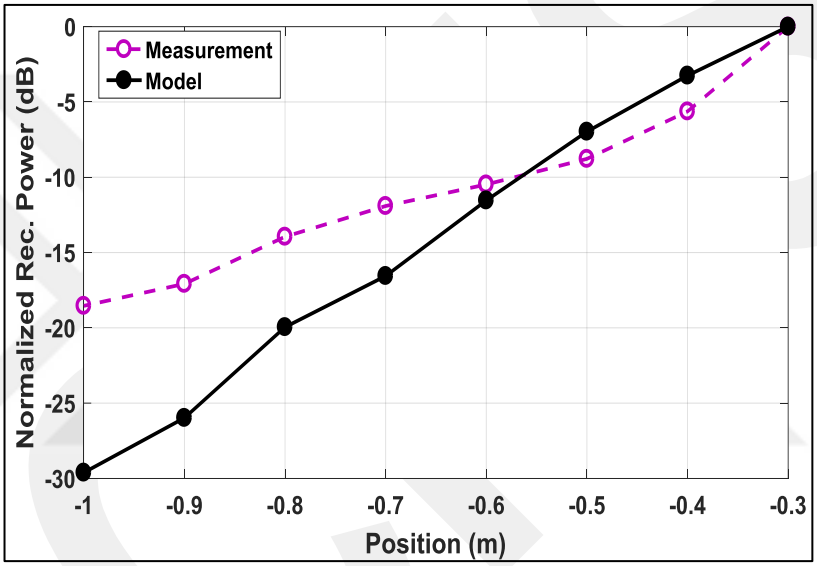

Figure 4.11. Comparison of the received power from measurements and the model simulation (scenario I).

4.4.2. Scenario II

Comparisons between the model simulation and the received power from measurements are made as shown in Figure 4.12. It can be observed that the model underestimates the measured received powers by 3–5 dB, which might be a of the vagueness in gains of the antennas (2–10 dB). The prediction accuracy of this model proves to be better than the specular reflection model of the metallic reflector.

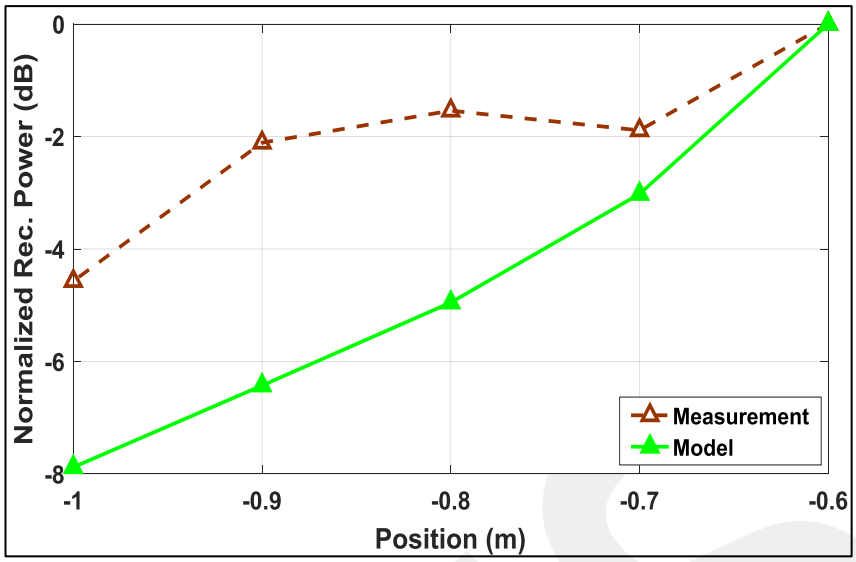

Figure 4.12. Comparison of the received power from measurements and the model simulation (Scenario II).

CHAPTER 5

CONCLUSIONS

In this study, measurements are carried out in order to study the effects of scattering objects close to the link at 28 GHz while the link are blocked by a human body. The scattering objects are a metallic reflector and human body. In order to predict the attenuation caused by the mentioned objects, reflection and diffraction modelling are used.

The basic mechanisms of wave propagation such as reflection and diffraction are calculated for each scattering object. To predict the attenuation caused by metallic reflector, the specular reflection model are employed in the reflection modelling. In the diffraction modelling, on the other hand, the double knife-edge diffraction (DKED) model are exploited to predict the attenuation by the human body. Simulations are then compared with measurements to evaluate the prediction accuracy of the models.

The results indicate that the attenuation resulted from the metallic reflector simulated by the specular reflection model that may be inaccurately predicted when the object is positioned away from the link. This may resulted from the antenna pattern gain and when conducting the measurement of the pattern gain, it has been found that the gain becomes considerably lower after 0.8 m away from the link (between 3 dB and -1 dB). Thus, the effect of the scattering object to the received power might be disregarded when it is away from the link.

It can be noticed in Scenario I that at certain points where the metallic reflector is close to the propagation link (between -0.3 m and -0.5 m) , the model exceeded the measured received powers by nearly 2 dB, while at other points, where the reflector is not close to the link, the model underestimated the measurements. It is noted that the blockage attenuation is significantly affected by the normalized gains of antennas.

In Scenario II, It can be observed that the model underestimates the measured received powers by 3–5 dB. This might be resulted from the vagueness in gains of antennas (2–10 dB). The prediction accuracy of this model proves to be better than the specular reflection model of metallic reflector.

As 5G communication may use millimetre wave bands, it is necessary to evaluate short-range indoor links from a link blockage point of view. On the other hand, only limited works have considered measurements to evaluate the effects of human blockage at 28 GHz. However, in this frequency band, no study has taken into account the effects of multiple blockages near the propagation link. In this context, to the best of our knowledge, the study presented in this thesis is the first report to provide a simple but accurate approach to characterize the effects of nearby objects around indoor links at 28 GHz while human body is fully blocking the link. The DKED model proved to be an ideal approach for predicting the attenuation caused by human body blockage. Consequently, the results achieved in this study will certainly provide a great perception for the modelling of people blocking links in future 5G systems.

Future work will contain more complex scenarios (number of peoples around the link and body types). Thus it will include more data processing, to provide an accurate human body model.

REFERENCES

[1] P. Sharma, "Evolution of mobile wireless communication networks-1G to 5G as well as future prospective of next generation communication network," *International Journal of Computer Science and Mobile Computing,* vol. 2, pp. 47-53, 2013.

[2] M. N. O. S. Kelechi, G. E. Sarhan and M. Musa, "5G Wireless Technology," in *International Journal of Scientific Engineering and Technology*, pp. 62-64, 2018.

[3] O. Breinbjerg and K. Kaslis, "On the accuracy of Friis' transmission formula at short range," in *2017 XXXIInd General Assembly and Scientific Symposium of the International Union of Radio Science (URSI GASS),* pp. 1-2, 2017.

[4] J. A. Dabin, N. Ni, A. M. Haimovich, E. Niver and H. Grebel, "The effects of antenna directivity on path loss and multipath propagation in UWB indoor wireless channels," in *IEEE Conference on Ultra Wideband Systems and Technologies,* pp. 305-309, 2003.

[5] T. S. Rappaport, *Wireless communications: principles and practice* vol. 2: prentice hall PTR New Jersey, 1996.

[6] A. Kara, "Human body shadowing variability in short-range indoor radio links at 3–11 GHz band," *International Journal of Electronics,* vol. 96, pp. 205-211, 2009.

[7] T. S. Rappaport, Y. Xing, G. R. MacCartney, A. F. Molisch, E. Mellios and J. Zhang, "Overview of millimeter wave communications for fifth-generation (5G) wireless networks—with a focus on propagation models," *IEEE Transactions on Antennas and Propagation,* vol. 65, pp. 6213-6230, 2017.

[8] X. Zhao, Q. Wang, S. Li, S. Geng, M. Wang, S. Sun, *et al.*, "Attenuation by human bodies at 26-and 39.5-GHz millimeter wavebands," *IEEE Antennas and Wireless Propagation Letters,* vol. 16, pp. 1229-1232, 2017.

[9] X. Chen, L. Tian, P. Tang and J. Zhang, "Modelling of human body shadowing based on 28 ghz indoor measurement results," in *2016 IEEE 84th Vehicular Technology Conference (VTC-Fall),* pp. 1-5, 2016.

[10] G. R. MacCartney, S. Deng, S. Sun and T. S. Rappaport, "Millimeter-wave human blockage at 73 GHz with a simple double knife-edge diffraction model

and extension for directional antennas," in *2016 IEEE 84th Vehicular Technology Conference (VTC-Fall)*, pp. 1-6, 2016.

[11] W. Qi, J. Huang, J. Sun, Y. Tan, C.X. Wang and X. Ge, "Measurements and modeling of human blockage effects for multiple millimeter Wave bands," in *2017 13th International Wireless Communications and Mobile Computing Conference (IWCMC)*, pp. 1604-1609, 2017.

[12] L. NiuYong, "A Survey of millimeterWave communications for 5G: Opportunities and challenges," *WirelessNetworks*, vol. 21, p. 2657, 2015.

[13] S. Singh, F. Ziliotto, U. Madhow, E. Belding and M. Rodwell, "Blockage and directivity in 60 GHz wireless personal area networks: From cross-layer model to multihop MAC design," *IEEE Journal on Selected Areas in Communications*, vol. 27, pp. 1400-1413, 2009.

[14] N. P. Lawrence, B. W.H. Ng, H. J. Hansen and D. Abbott, "5G terrestrial networks: Mobility and coverage—Solution in three dimensions," *IEEE Access*, vol. 5, pp. 8064-8093, 2017.

[15] X. Tan, Z. Sun, D. Koutsonikolas and J. M. Jornet, "Enabling indoor mobile millimeter-wave networks based on smart reflect-arrays," in *IEEE INFOCOM 2018-IEEE Conference on Computer Communications*, pp. 270-278, 2018.

[16] D. Liu and R. Sirdeshmukh, "A patch array antenna for 60 GHz package applications," in *2008 IEEE Antennas and Propagation Society International Symposium*, pp. 1-4, 2008.

[17] J. Lucas, "What Is Electromagnetic Radiation?," ed. https://www.livescience.com/38169-electromagnetism.html, 2015.

[18] A. Alabish, A. Kara, and Y. Dalveren, "An Experimental Study towards Examining Human Body Movements in Indoor Wave Propagation at 18–22 GHz," in *2018 International Symposium on Networks, Computers and Communications (ISNCC)*, 2018, pp. 1-4.

[19] M. Williamson, G. Athanasiadou, and A. Nix, "Investigating the effects of antenna directivity on wireless indoor communication at 60 GHz," in *Proceedings of 8th International Symposium on Personal, Indoor and Mobile Radio Communications-PIMRC'97*, 1997, pp. 635-639.

[20] J. D. Parsons and P. J. D. Parsons, "The mobile radio propagation channel," 1992.

[21] H. G. Kraus, "Huygens–Fresnel–Kirchhoff wave-front diffraction formulation: spherical waves," *JOSA A*, vol. 6, pp. 1196-1205, 1989.

[22] L. Boithias, "Radio Wave Propagation,(trans. to English by D. Beeson) McGraw-Hill," *New York*, 1987.

[23] M. E. Brezinski, *Optical coherence tomography: principles and applications*: Elsevier, 2006.

[24] G. Koutitas, *Advanced physical techniques for radio channel modeling*: University of Surrey (United Kingdom), 2007.

[25] F. P. Fontan, A. Abele, B. Montenegro, F. Lacoste, V. Fabbro, L. Castanet, *et al.*, "Modelling of the land mobile satellite channel using a virtual city approach," in *The Second European Conference on Antennas and Propagation, EuCAP*, pp. 1-7, 2007.

[26] J. Medbo and F. Harrysson, "Channel modeling for the stationary UE scenario," in *2013 7th European Conference on Antennas and Propagation (EuCAP)*, pp. 2811-2815, 2013.

[27] J. Kunisch and J. Pamp, "Ultra-wideband double vertical knife-edge model for obstruction of a ray by a person," in *2008 IEEE International Conference on Ultra-Wideband*, pp. 17-20, 2008.

[28] G. L. James, *Geometrical theory of diffraction for electromagnetic waves*: IET, 1986.

[29] P. Pagani and P. Pajusco, "Characterization and modeling of temporal variations on an ultrawideband radio link," *IEEE Transactions on Antennas and Propagation*, vol. 54, pp. 3198-3206, 2006.

[30] H. L. Bertoni, *Radio propagation for modern wireless systems*: Pearson Education, 1999.

[31] P. Karadimas, B. Allen and P. Smith, "Human body shadowing characterization for 60-GHz indoor short-range wireless links," *IEEE Antennas and Wireless Propagation Letters*, vol. 12, pp. 1650-1653, 2013.

[32] T. Wu, T. S. Rappaport and C. M. Collins, "The human body and millimeter-wave wireless communication systems: Interactions and implications," in *2015 IEEE International Conference on Communications (ICC)*, pp. 2423-2429, 2015.